International Journal of Biological Macromolecules 235 (2023) 123821

Contents lists available at ScienceDirect

International Journal of Biological Macromolecules

journal homepage: www.elsevier.com/locate/ijbiomac

Cancer-targeted fucoidan-iron oxide nanoparticles for synergistic chemotherapy/chemodynamic theranostics through amplification of P-selectin and oxidative stress

Thi-Luu Ho [a,b], Chinmaya Mutalik [c], Lekshmi Rethi [c], Huynh-Ngoc Truc Nguyen [a], Pei-Ru Jheng [a,c], Chin-Chean Wong [d,e,f,g], Tzu-Sen Yang [h], Thi Thuy Nguyen [i,j], Bradley W. Mansel [k], Chen-An Wang [k], Er-Yuan Chuang [a,c,l,*]

[a] Graduate Institute of Biomedical Materials and Tissue Engineering, College of Biomedical Engineering, Taipei Medical University, Taipei 11031, Taiwan
[b] International Ph.D. Program for Cell Therapy and Regeneration Medicine, College of Medicine, Taipei Medical University, Taipei 110, Taiwan
[c] International Ph.D. Program in Biomedical Engineering, College of Biomedical Engineering, Taipei Medical University, Taipei 11031, Taiwan
[d] Department of Orthopedics, Shuang Ho Hospital, Taipei Medical University, New Taipei City 23561, Taiwan
[e] Department of Orthopedics, School of Medicine, College of Medicine, Taipei Medical University, Taipei 11031, Taiwan
[f] Research Center of Biomedical Devices, Taipei Medical University, Taipei 11031, Taiwan
[g] International Ph.D. Program for Cell Therapy and Regenerative Medicine, College of Medicine, Taipei Medical University, Taipei 11031, Taiwan
[h] Graduate Institute of Biomedical Optomechatronics, College of Biomedical Engineering, Taipei Medical University, Taipei 11031, Taiwan
[i] International Ph.D. Program in Medicine, College of Medicine, Taipei Medical University, Taipei 11031, Taiwan
[j] Department of Oncology, Hue University of Medicine and Pharmacy, Hue University, Hue, Viet Nam
[k] National Synchrotron Radiation Research Center, Hsinchu 30076, Taiwan
[l] Cell Physiology and Molecular Image Research Center, Taipei Medical University-Wan Fang Hospital, Taipei 11696, Taiwan

ARTICLE INFO

Keywords:
Synergistic chemotherapy/chemodynamic theranostics
Amplification of P-selectin and oxidative stress
Cancer-targeted fucoidan-iron oxide nanoparticles

ABSTRACT

A combination of chemotherapy and chemodynamic therapy (CDT) is being developed to improve the theranostic efficacy and biological safety of current therapies. However, most CDT agents are restricted due to complex issues such as multiple components, low colloidal stability, carrier-associated toxicity, insufficient reactive oxygen species generation, and poor targeting efficacy. To overcome these problems, a novel nanoplatform composed of fucoidan (Fu) and iron oxide (IO) nanoparticles (NPs) was developed to achieve chemotherapy combined with CDT synergistic treatment with a facile self-assembling manner, and the NPs were made up of Fu and IO, in which the Fu was not only used as a potential chemotherapeutic but was also designed to stabilize the IO and target P-selectin-overexpressing lung cancer cells, thereby producing oxidative stress and thus synergizing the CDT efficacy. The Fu-IO NPs exhibited a suitable diameter below 300 nm, which favored their cellular uptake by cancer cells. Microscopic and MRI data confirmed the lung cancer cellular uptake of the NPs due to active Fu targeting. Moreover, Fu-IO NPs induced efficient apoptosis of lung cancer cells, and thus offer significant anti-cancer functions by potential chemotherapeutic-CDT.

1. Introduction

Chemodynamic therapy (CDT), a reactive oxygen species (ROS)-boosting strategy for curing cancer, focuses on eradicating cancer cells with excessive ROS, such as hydroxyl radicals (·OH) [1]. CDT is principally dependent on the Fenton-like or Fenton reaction for catalyzing less-harmful hydrogen peroxide (H_2O_2) in an acidic microenvironment to ·OH, the most toxic ROS, to cause damage and apoptosis to cancer cells [1–3]. Crucial aspects of the CDT procedure are an acid microenvironment, transitional metals, and H_2O_2. Thus, despite the advantages of features of cellular H_2O_2 overexpression of the microenvironment and acidity, CDT is being extensively investigated as a more-specific treatment against cancer with independent inputs of either exterior energy or oxygen, and synchronously with no consideration of limitations of the

* Corresponding author at: Graduate Institute of Biomedical Materials and Tissue Engineering, College of Biomedical Engineering, Taipei Medical University, Taipei 11031, Taiwan.
E-mail address: eychuang@tmu.edu.tw (E.-Y. Chuang).

https://doi.org/10.1016/j.ijbiomac.2023.123821
Received 20 September 2022; Received in revised form 17 February 2023; Accepted 19 February 2023
Available online 2 March 2023

penetrating depths of lasers into organs [4].

However, after extensive study of CDT approaches, scientists gradually noted that awkward challenges still persisted before agreeable therapeutic uses could be achieved. First, the limitation of cellular H_2O_2 inside tumor tissues (0.1– 1 mM) caused an undesirable CDT process and an unsatisfactory efficiency of ·OH generation [1]. Another limitation derived from the constraint of the rigorous reaction conditions (pH 2– 4) [1,5] and a slower chemical reaction rate (ca. 63 M^{-1}/s) [5] of the most-often employed ferric-based CDT substances (such as iron oxide, IO). The third was associated with a rise in ROS-shielding mechanisms [4,6], mainly regarding glutathione (GSH) (1– 10 mM within tumor cells) [7,8]. Furthermore, these CDT-based inorganic nanoparticles (NPs) were largely prevented from clinical translation because of their complex preparation procedures, poor colloidal stability and reproducibility, a lack of tumor tissue selectivity, and particularly their potential systemic toxicity [9].

These aspects revealed the challenges encountered when enhancing curative effects through CDT. To address these essential concerns and acquire augmented anticancer theranostic efficiencies, an ideal theranostic nanoplatform should have the following features: (i) a straightforward and additional manner for sufficient ROS generation in tumors; (ii) excellent colloidal biocompatibility and stability, and notable tumor-targeting capacity for improving CDT efficacy; and (iii) combinational ROS formation and GSH depletion in one nanoplatform to advance the accumulation of ROS and augment the effect of ROS-facilitated therapies.

Recently, fucoidan (Fu) has attracted the attention of scientists in multidisciplinary areas, including biomaterials, nanomedicine, and anticancer [10–13]. Fu is a biocompatible, sulfated polysaccharide that can be used in nano-formulations with hydrophobic therapeutic agents to increase their colloidal stability [14]. Synthesis of a Fu-based drug carrier system can minimize the side effects of the chemo drug and facilitate the active targeting and delivery efficacy toward P-selectin-overexpressing cancer cells [15–17]. Moreover, Fu is considered a natural chemotherapeutic agent due to its exhibited characteristics [10,11]. Fu-induced cancer cell death and anti-metastasis action are related to the depletion of GSH, an accumulation of high cellular ROS levels, and accompanying damage to mitochondrial structures, caspase bioactivation, and depolarization of the mitochondrial membrane potential (MMP) [11,18]. Fucoidan can induce apoptosis and antitumor activity via ROS-dependent c-Jun N-terminal kinase (JNK) inhibition and mitochondrial-mediated pathways [19], as well as reduction of Wnt/beta-catenin signaling [20], and the hypoxia-inducing factor (HIF)-1 signaling pathway [21]. After 72 h of treatment, Fu decreased the proliferation of breast cancer cells (MDA-MB-231 cell line) by 53.2 % at a 25 μg/mL concentration [21].

Herein, we designed a Fu-IO therapeutic nano-system using a facile co-precipitation procedure to produce IO and then wrap the Fu onto the IO surface through ionic interactions. In this nano-system, Fu acted as an intelligent shell to effectively enhance colloidal stability and the cancer-targeting efficacy of the CDT IO NPs (Fu-IO NPs) through P-selectin mediation, thus avoiding adverse effects. When the nanomedicine was enriched in cancer cells through P-selectin mediation, the accumulation of Fu-IO NPs in cancer cells could be detected by magnetic resonance (MR) imaging (MRI) from a diagnostic aspect. This is commonly used as a real-time clinical diagnostic tool for differentiating cancer cells because of its benefits of noninvasiveness, deep tumor penetration, and multiparametric imaging [9]. Thus, cancer cell-targeted MRI with the use of contrast agents is of great interest for distinguishing abnormal regions from normal cells. We assessed the physicochemical properties, in vitro and in vivo cellular uptake efficiency, toxicity, and theranostic efficacy of Fu-IO NPs. We hypothesized that these self-assembling multifunctional Fu-IO NPs possessed specific cancer targeting, good MRI ability, and a significant anticancer effect. The increased cancer cellular uptake of Fu-IO NPs was hypothesized to augment the CDT process and enhance Fu's biological effects, including increasing cellular ROS and depleting GSH, thus synergizing the CDT anticancer effect of IO. Therefore, combined therapy with Fu and CDT could be achieved with this precise cancer microenvironment-responsive nanosystem, which presented an excellent theranostic effect of suppressing lung cancer growth and metastasis (Scheme 1).

2. Experimental section

2.1. Materials

Fu (*Fucus serratus*, 95 % purity, from *Alaria esculenta*) was purchased from the Taiwanese agent of Biosynth Carbosynth (Taipei, Taiwan). The fucose content of this fucan was ca. 37.5 %, and it also contained galactose (ca. 16.4 %), uronic acid (ca. 12.3 %), and sulfate (ca. 20.2 %). High-glucose Dulbecco's modified Eagle medium (DMEM) and high-glucose minimum essential medium (MEM) supplemented with L-glutamine and 10 % fetal bovine serum (FBS) were obtained from Gibco (Grand Island, NY, USA). Iron (III) chloride ($FeCl_3$, 97 %), polyethylenimine (PEI, branched, average Mw ~800 by LS), and 3,3′,5,5′-tetramethylbenzidine (TMB) liquid substrate system for an enzyme-linked immunosorbent assay (ELISA) were from Sigma-Aldrich (St. Louis, MO, USA). Iron (II) chloride ($FeCl_2$, anhydrous, 99.5 %) was purchased from Alfa Aesar (Ward Hill, MA, USA). 2′,7'-Dichlorofluorescin diacetate (H2DCFDA) and CellTracker™ Green CMFDA Dye (Invitrogen™) were bought from ThermoFisher Scientific (Waltham, MA, USA). Other chemicals and reagents in this work were of analytical grade and were procured from Sigma-Aldrich (St. Louis, MO, USA) unless otherwise stated.

2.2. Preparation of the nanoformulations

2.2.1. Synthesis of IO NPs

IO NPs were prepared by co-precipitation of an iron chloride salt method [22]. Briefly, $FeCl_3$ (250 mg) and $FeCl_2$ (97.6 mg) were dissolved in double-distilled (dd) water under stirring at 70 °C, and 1 M NaOH was then added drop-by-drop. Under stirring, the appearance of black precipitates with time indicated the formation of IO NPs. The materials were collected with a magnet, washed three times with dd water, and then dried by lyophilized-freezing for subsequent steps.

2.3. Preparation of Fu-IO NPs

To change the charge of the IO NPs, polyethylenimine (PEI) was used to coat the IO NPs according to a previous paper [23]. First, a sonicated IO NP solution was added drop-by-drop to a PEI solution under stirring. After being sonicated for 20 min, the PEI-IO NP mixture was continuously stirred for 2 h. This solution was dialyzed for 2 days to remove any excess PEI. The PEI-IO NPs were precipitated by centrifugation and cleaned three times with dd water. The Fu-IO NPs were fabricated by an electrostatic method according to the literature [24]. Fu (1 mg/mL) was dissolved in dd water with stirring at 50 °C until a light yellowish, homogenous solution was obtained. Then, the above-synthesized PEI-IO NP solution was put dropwise into the Fu solution under vigorous stirring at 50 °C for a further 2 h. Finally, Fu-IO NP pellets were collected using a centrifuge machine (Purispin 17R Micro, Cryste, Korea) at 15,000 rpm for 10 min.

2.4. Physicochemical characterization of the NPs

2.4.1. Fourier-transform infrared (FTIR) spectroscopy

Powdered samples of IO NPs, Fu, and Fu-IO NPs were tested on an FTIR spectrometer (Nicolet iS10, ThermoFisher Scientific). Multiple scans of 100 s were used to record FTIR spectral changes of samples in the 4000– 500 cm^{-1} wavenumber range.

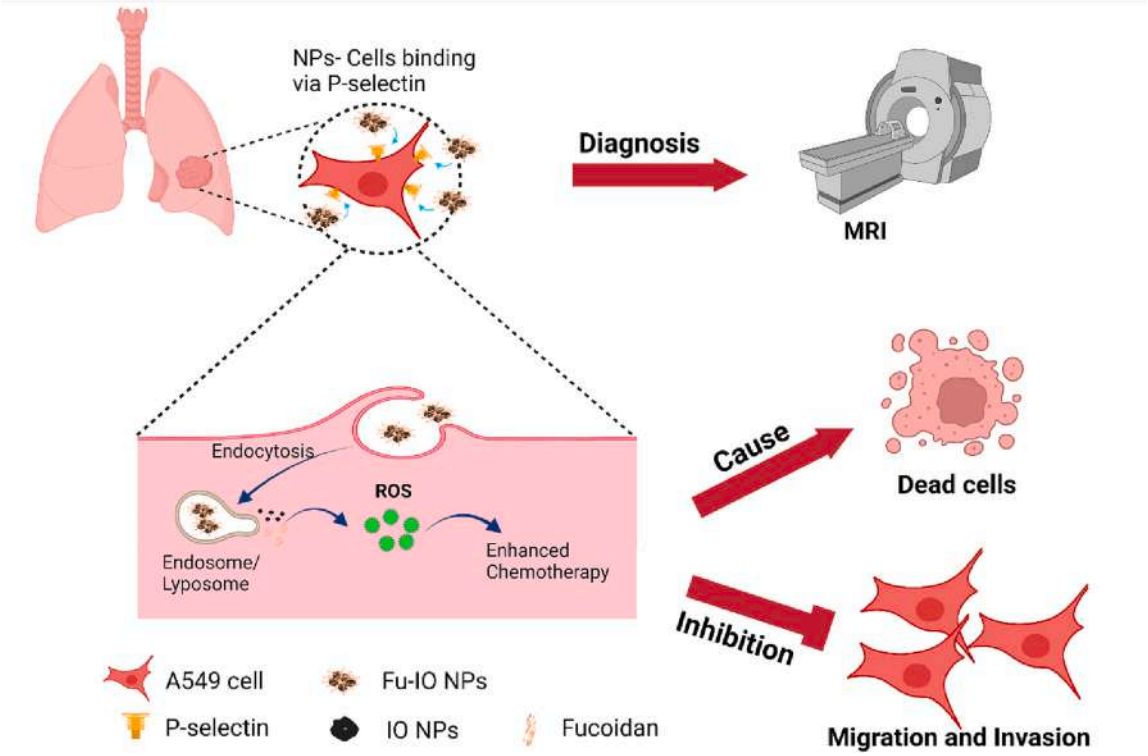

Scheme 1. Schematic illustration of the nanoscale reactive oxygen species (ROS) generator fucoidan-iron oxide nanoparticles (Fu-IO NPs) which possess potential for application in MRI-guided lung cancer theranosis by synergizing chemotherapy-chemodynamic therapy (CDT).

2.4.2. X-Ray diffraction (XRD) analysis

Powdered samples of IO NPs, Fu, and Fu-IO NPs were placed on a D2 XRD instrument (Bruker AXS, Madison, WI, USA). The angle range was set from 10° to 40° with a 0.05° step size and 4-s integration for a wide-angle scan.

2.4.3. Elemental analysis

To prove the successful fabrication of NPs, material elements of the samples were analyzed using a scanning electron microscopy/energy-dispersive x-ray spectroscopy (SEM–EDS) analysis (SEM SU3500v, Hitachi Tokyo, Japan). The NPs were dispersed onto carbon tape at 1.5 kV, and the data collecting time was 90– 120 s depending on the signal.

2.4.4. Transmission electron microscopy (TEM)

IO NP and Fu-IO NP morphologies, including the particle size and shape, were determined using TEM (HT7700, Hitachi, Tokyo, Japan). One drop of an NP dispersion was placed on a carbon-supported copper grid of a 200-mesh size and dried at approximately 60 °C in an oven. This step was carried out three times.

2.4.5. Small-angle X-ray scattering (SAXS)

SAXS was performed on a beamline 13A of the Taiwan Photon Source (TPS) storage ring at National Synchrotron Radiation Research Center (NSRRC) [25,26]. A 15-keV incident x-ray beam was used with an Eiger X1M detector (Dectris, Baden-Daettwil, Switzerland) located 3018.9 mm from the sample. Multiple 1-s exposures were recorded at room temperature as the sample and background flowed through a capillary cell, followed by averaging and background subtraction. Data processing was performed using the standard beamline software, which includes pyFAI [27]. The scattering intensity was measured as a function of the scattering vector $q = |q| = 4\pi sin(\theta/2)/\lambda$; where θ is the scattering angle, and λ is the wavelength. Model fitting of the Guinier-Porod model was performed using SASView 4.2.2.

2.4.6. Particle size analysis and surface charge

The size distribution and zeta potential of the IO NPs and Fu-IO NPs were determined by an NP tracking analysis (Nanosight NS300, Malvern Instruments, Amesbury, UK) and a dynamic light scattering (DLS) method (ZetaSizer Nano Series, Malvern Instruments), respectively. Stock NP solutions were dissolved in dd water or phosphate-buffered saline (PBS; at pH 7.4) at the optimum concentration for the sample analysis.

2.5. Determination of the Fu and iron contents inside the Fu-IO NPs

In this study, quantification of Fu in Fu-IO NPs was determined with a methylene blue colorimetric assay [28]. A Fu-IO NP sample was mixed with a methylene blue solution (0.5 mL, 25 μg/mL). Then, the absorbance of test samples was measured at 559 nm using an ultraviolet-visible (UV–Vis) spectrophotometer (Jasco V-770 spectrophotometer, Easton, MD, USA) ($n = 3$). Various known concentrations of Fu were mixed with the methylene blue solution (0.5 mL, 25 μg/mL) and measured by UV–Vis to generate a standard curve.

We performed a Prussian blue reaction as a colorimetric assay to quantify the amount of IO [29]. Briefly, various known concentrations of IO NPs were incubated with Perl's reagent (2 % potassium ferrocyanide/ 2 % HCl, 1:1, v/v) for 30 min. Then, these solutions were measured with a UV–Vis spectrophotometer (Jasco V-770 spectrophotometer) at 570 nm to create a standard curve. The iron contents of the Fu-IO NP samples were calculated based on the above standard curve.

2.6. Colloidal stability study

IO NPs and Fu-IO NPs colloids were placed in plastic cuvettes at room temperature for 7 days. To observe the color changes or whether the colloids precipitated, images of the colloidal NPs were taken with a camera every day. Moreover, the particle size and zeta potential of prepared NPs were measured on day 1 and day 7 by a dynamic light scattering (DLS) method (ZetaSizer Nano Series, Malvern Instruments).

2.7. In vitro studies

2.7.1. Cell culture

The HEL 299 cell line (normal fibroblast cells) at passage 15 was seeded in MEM containing Earle's salts and L-glutamine, and 10 % FBS and 1 % of penicillin/streptomycin/amphotericin-B (PSA) were added. The A549 cell line at passage 20 was cultured in high-glucose with sodium pyruvate DMEM supplemented with 10 % FBS and 1 % PSA. Cells were cultured in a standard cell incubator with a humidified 5 % CO_2 atmosphere at 37 °C. The culture medium was changed every 2– 3 days when cells had surpassed 90 % confluency.

2.7.2. Cell P-selectin expression analysis

Herein, HEL 299 and A549 cells were cultured on confocal dishes (35 × 10 mm) at 4 × 10^4 cells/dish until confluent. Cells were fixed with 4 % paraformaldehyde and 0.2 % Triton X-100, respectively, every 10 min at 37 °C. Subsequently, cells were treated with an anti-P-selectin/CD62P antibody conjugated with phycoerythrin (PE) (AK-6, Abcam, Cambridge, UK) overnight at 4 °C. After several washes with PBS, their nuclei were counterstained with DAPI. To determine expression of the P-selectin protein by HEL 299 and A549 cells, cells were examined with fluorescence microscopy (Leica Microsystems, Mannheim, Germany).

2.7.3. Measurement of ROS production

ROS production by HEL 299 and A549 cells was detected using 2′,7′-dichlorofluorescein diacetate (H2DCFDA) staining [1]. Cells were seeded on 96-well plates until reaching 90 % confluency and then treated with IO NPs (100 μg/mL), Fu (15 μg/mL), and Fu-IO NPs (equivalent to 100 μg/mL IO NPs and 15 μg/mL Fu) for 6, 24, and 48 h. The control group consisted of cells incubated with fresh medium only. Fluorescence microscopy (Leica Microsystems) was used to record the signal of the generated dichlorofluorescein (DCF), a green color. The fluorescence intensity was quantitated using ImageJ 1.53 k software (National Institutes of Health (NIH), Bethesda, MD, USA).

2.7.4. Glutathione (GSH) depletion assay

A549 cells were seeded in confocal dishes until confluency and then treated with IO NPs (100 μg/mL), Fu (15 μg/mL), and Fu-IO NPs (equivalent to 100 μg/mL IO NPs and 15 μg/mL Fu) for 6 h, 24 h, and 48 h. The control group consisted of cells incubated with fresh medium only. After that, cells were washed with BPS 3 times and stained with 5 mM 5-chloromethylfluorescein diacetate (CMFDA) for 30 min at 37 °C. Finally, the cells were washed with BPS before detecting the GSH signal by Fluorescence microscopy (Leica Microsystems).

2.7.5. In vitro cellular uptake

To estimate the cellular uptake of the prepared NPs, A549 cells were stained with Prussian blue [30]. Briefly, cells treated with IO NPs (100 μg/mL), Fu (15 μg/mL), and Fu-IO NPs (equivalent to 100 μg/mL IO NPs and 15 μg/mL Fu), or DMEM were incubated for 6, 24, or 48 h. Cells were rinsed with PBS and stained with freshly prepared Perl's reagent (2 % potassium ferrocyanide/2 % HCl, 1:1, v/v) for 30 min. Cells were washed with PBS before being counterstained with neutral red solution (0.33 %) for 30 s. Subsequently, stained cells were observed with an optical microscope (Leica Microsystems) to evaluate the intracellular iron distribution.

To obtain specific data on the uptake and internalization of the prepared NPs by cells, TEM images were employed. Briefly, A549 cells were seeded on two-well chamber slides (4.2 cm^2/well) until 80 % confluent. After 6 h, 8 h, 12 h, and 24 h of incubation with Fu-IO NPs, cells were washed with PBS to remove the excess NPs and fixed with 3 % glutaraldehyde in 0.1 M cacodylate buffer (pH 7.3) for 30 min. Post-fixed cells were rinsed again with PBS and were kept at 4 °C for 1 day. After that, cells were subjected to a dehydrating process with an ethanol series before infiltration-embedding with epoxy resin. Finally, images of cellular uptake were visualized with an HT7700 TEM instrument (Hitachi).

In order to determine the suitability of Fu-IO NPs as MRI contrast agents, HEL 299 and A549 cells were treated with IO NPs (100 μg/mL), Fu (15 μg/mL), and Fu-IO NPs (equivalent to 100 μg/mL IO NPs and 15 μg/mL Fu) for 6, 24, and 48 h. Cells were then rinsed with PBS three times to remove excess NPs and were detached with trypsin-EDTA. After that, cells were suspended in a 1 % agarose gel solution. MR images of agarose/cell/NP gels were acquired on a 7 T MRI instrument (Pharma Scan, Bruker BioSpin, Billerica, MA, USA).

2.7.6. MTT assay

HEL 299 and A549 cells were seeded at the density of 10^5 cells/mL (100 μL per well) in 96-well plates to grow until confluent. Serial concentrations of Fu-IO NPs in HEL 299 cells or IO NPs (100 μg/mL), Fu (15 μg/mL), and Fu-IO NPs (equivalent to 100 μg/mL IO NPs and 15 μg/mL Fu) in A549 cells were incubated with cells for different time points (6, 24, and 48 h). The control group consisted of cells cultured with 100 % fresh medium. After washing cells several times with PBS, fresh medium was added. Subsequently, cells were immersed in an MTT solution (20 μL, 1 mg/mL) for approximately 2 h. Finally, the supernatant medium was decanted, and a dimethyl sulfoxide (DMSO) solution was added to extract the formazan crystals that had formed. Their optical absorbance at 570 nm was measured with an ELISA reader (Multiskan FC; Thermo, Waltham, MA, USA) (n = 4). Medium only or medium containing different concentrations of NPs without cells was respectively used as blank samples for the control and test groups. Finally, cell viability was determined and calculated using the equation:

$$Cell\ Viability(\%) = \frac{Asample–Asampleblank}{Acontrol–Acontrolblank} \times 100\%.$$

2.7.7. Live/dead cell assay

In this study, we performed a live/dead cell assay to qualitatively assess the biochemical effects of the NPs on cell viability. A549 cells were cultured with 2 × 10^4 cells/well on 24-well plates until 80 % confluency was reached. After 48 h of co-incubation with IO NPs (100 μg/mL), Fu (15 μg/mL), and Fu-IO NPs (equivalent to 100 μg/mL IO NPs and 15 μg/mL Fu), cells were stained with a Live and Dead Assay Kit following the protocol of Abcam (Cambridge, UK). Finally, cells were examined with a fluorescence microscope. The experiment was conducted with triplicate determinations (n = 3).

2.7.8. Migration (scratch-wound) assay

To evaluate the effect of NPs on the inhibition of cancer cell migration/metastasis in vitro, a scratch-wound assay was conducted [21]. A549 cells were seeded in six-well plates until confluent. Following treatment with IO NPs (100 μg/mL), Fu (15 μg/mL), and Fu-IO NPs (equivalent to 100 μg/mL IO NPs and 15 μg/mL Fu) for 48 h, cells were scratched using a sterile 200-μl pipette tip, and dead cells were washed away with PBS. After that, cells were continually incubated with fresh medium. Five images of cell migration were captured from randomly selected microscopic fields at 0, 6, and 24 h. The area of cell migration was determined using ImageJ 1.53 k software (NIH) and the percentage of the migrated area was computed by the following equation:

$$\%Migrated\ area = \frac{Scratch\ area\ at\ zero\ time - scratch\ area\ at\ specific\ time}{Scratch\ area\ at\ zero\ time} * 100.$$

2.7.9. Cell-invasion assay

A cell-invasion assay was performed to assess NP inhibition of the invasive behavior of A549 cells using a 24-well transwell chamber [31]. A549 cells (2 × 10^5 cells/mL, 0.1 mL) were treated with prepared NPs for 48 h. Cells were then harvested, resuspended in fresh medium, and seeded onto the Matrigel-coated (BD Biosciences, San Jose, CA, USA) upper chamber. To the lower chamber was added 750 μL of culture medium in the absence or presence of NPs. After 48 h of incubation, non-

invading cells on the upper side were removed, while invading cells on the lower surface were fixed in 4 % paraformaldehyde for 15 min and stained with 0.2 % crystal violet for 1 h. Finally, we used a microscope and ImageJ software (NIH) to record and count the number of invading cells on the lower surface.

2.8. In vivo studies

Approval for the animal experiments was acquired from the Institutional Animal Care and Use Committee at Taipei Medical University (IACUC TMU). Immunodeficient mice weighing 18–24 g (6–8 weeks old) were obtained from BioLASCO Taiwan (Taipei, Taiwan) To create an in vivo tumor model, A549 cells were subcutaneously injected into mice. The experiments were performed after tumor formation (50– 150 mm^3). NPs were used to evaluate the in vivo biodistribution and antitumor efficacy by measuring tumor volume change. A549 tumors in these mice were injected with NPs. The mice were anesthetized with isoflurane and photographed with a 7 T MRI instrument (Pharma Scan, Bruker BioSpin, Billerica, MA, USA). After the mice were euthanized with carbon dioxide, the major organs (heart, liver, spleen, lungs, and kidneys) and tumors were excised, immersed in 4 % paraformaldehyde and embedded in paraffin before tissue sectioning. After DCFDA, Prussian blue, or hematoxylin and eosin (H&E) staining, histological changes of the organs were observed by microscopy.

2.9. Statistical analysis

Statistical analyses were performed using Graph Pad Prism v6.01 (Graph Pad Software, La Jolla, CA, USA), Origin Pro 8.5 program (Origin Lab, Northampton, MA, USA), and ImageJ 1.53 k software (NIH). Statistical analyses included a two-way analysis of variance (ANOVA) followed by Dunnett's multiple-comparison test. All data are presented as the mean ± standard deviation (SD). Values of $^{*}p < 0.05$, $^{**}p < 0.01$, $^{***}p < 0.001$ and $^{****}p < 0.0001$ were considered statistically significant.

3. Results and discussion

3.1. Preparation and characterization of the nanoformulations

To evaluate the successful fabrication of NPs, physicochemical analyses were carried out. Molecular structural changes of the samples were analyzed using an FTIR spectrophotometer. Fig. 1A illustrates the FTIR spectra of IO NPs, Fu, and Fu-IO NPs. There were peaks at 539 and 564 cm^{-1} in the spectrum of IO NPs and Fu-IO NPs, respectively. These peaks corresponded to Fe—O bond formation [32]. However, the magnetic core of the Fu-IO NPs was coated with Fu resulting in a less-intense peak. As observed in all spectra, the absorption peak at about 3300 cm^{-1} may have been due to hydroxyl (OH) present in the water or polysaccharides. The bands at around 800 (C—O—S stretching vibrations), 1019 (C—O—C stretching vibrations), and 1200 cm^{-1} (S═O stretching vibrations) were observed in IO NP and Fu-IO NP spectra, confirming that Fu had successfully been coated onto the IO NP surfaces.

To better understand the impact of the Fu-coated surface on IO NPs, XRD patterns of the prepared NPs were measured. Bare IO NPs, Fu, and Fu-IO NPs were scanned with an XRD instrument (Bruker) within the 2θ range of 30° ~ 80° to determine the crystallographic planes of the Fu-capped nanomaterials (Fig. 1B). Furthermore, with regard to the XRD diffractograms of IO NPs, a series of characteristic peaks at 311, 400, 422, 511, 440, and 533 was observed. These results were similar to the Fe_3O_4 structure (magnetite, JCPDS card no. 85-1436) [33]. The Fu-IO NP diffractogram also showed the same peaks as IO NPs, suggesting that functionalization did not degrade the core magnetite. As a result, the present methodology was found to be successful in producing Fu-capped IO NPs.

The chemical elements of the prepared IO NPs and Fu-IO NPs were analyzed using SEM-EDX. In Fig. 1C and D, peaks of the Fe and O elements were observed to exhibit good stoichiometry. Moreover, Fig. 1D shows the presence of C, N, and S elements, which possibly came from PEI and/or Fu compounds. It is worth noting that Fu-coated IO NPs were successfully tested. In addition, the elemental mapping analysis further confirmed the homogeneous presence of elements from the prepared NPs.

SAXS was used to characterize the NP structures at length scale between those accessible with XRD and dynamic light scattering (DLS). SAXS data, as revealed in Fig. 1E, showed that the NPs were composed of clusters of smaller primary particles assembled to produce fractal structures. The data showed two different linear slopes on a log-log plot indicating the fractal dimension of the internal structure of the associated NPs at $q < 0.04$ $Å^{-1}$ together with a surface fractal related to a polydispersed primary particle size and surface roughness at higher q values. To quantify these two slopes, the Guinier-Porod (GP) model was utilized [34], which revealed that while the overall structures of the IO and Fu-IO NPs were highly similar, the low-q fractal structure of Fu-IO NPs was 2.289 ± 0.0002 compared to 2.146 ± 0.0002 for IO NPs. The model extracted radii of gyration (Rg) of 11.7 ± 0.008 and 13.8 ± 0.007 Å with high-q surface fractals of 3.51 ± 0.001 and 3.5 ± 80.009 for the Fu-IO and IO NPs, respectively. It should be noted that due to the broad size distribution, a true Rg could not be defined, although such a transition from a mass fractal to a surface fractal is generally indicates of the primary particle size in NP clusters [35]. SAXS showed that the primary particles were polydispersed in size and morphology with little difference between the Fu-IO and IO primary particles, although differences in the low-q fractal slopes revealed differences in the internal structure of the assembled particles.

The particle size and zeta potential of NPs influence their behavior in terms of biosafety and biological activity [36,37]. It is crucial to understand the qualities of the NPs produced. Herein, we validated the size and zeta-potential of NPs in water and PBS (pH 7.4), mimicking the physiological microenvironment. As shown in Fig. 2A, IO NP mean sizes significantly increased from ca. 49 nm in water (upper) to ca. 116 nm in PBS (lower), which induced the instantaneous aggregation of IO NPs in the biological environment. In contrast, the sizes of Fu-IO NPs (Fig. 2B) in water (ca. 143 nm) (upper) and in PBS (ca. 122 nm) (lower) exhibited a slight change, which may have been caused by an error in the NTA measurement. The presence of a coated Fu surface on Fu-IO NPs inhibited agglomeration or contact between bare IO NPs, as demonstrated by these data. This indicates that the Fu-IO NPs were colloidally stable in the physiological environment. Moreover, as expected, the zeta potentials of the prepared IO NPs and Fu-IO NPs dramatically increased in PBS by ca. 15 and ca. 8 mV (Fig. 2C, D), respectively, which would facilitate greater cellular uptake of the NPs [38].

Aside from that, IO NPs were first synthesized with a negative charge. Then, PEI added cationic groups which acted as linkers by providing positively charged functional groups onto the negatively charged IO surface. Then, solid electrostatic interactions between PEI (NH_3^+) and Fu (SO_3^-) facilitated the Fu being coated onto the PEI-IO surface. As the results show (Fig. S1), the zeta potentials of IO NPs, PEI-IO NPs, and Fu-IO NPs were around −34, 26, and −13 mV, respectively. Moreover, the average sizes of IO NPs, PEI-IO NPs, and Fu-IO NPs were measured by DLS in the water phase.

Morphological changes in IO NPs and the Fu-IO NPs were observed by TEM (Fig. 3A). IO NPs were polydispersed and had rock-like crystallized structures with an average diameter of 9.56 ± 2.02 nm ($n = 30$) (Fig. 3A, left side). The measured size from TEM images was smaller than that from NTA measurements due to the former preparation of samples fundamentally differing from the latter. Moreover, TEM images showed an agglomeration of bare IO NPs. As a result, NTA values for IO NP sizes might not have accounted for single IO NPs. In addition, TEM images of Fu-IO NPs showed their size to be ca. 105.6 ± 37.14 nm, and they were well dispersed (Fig. 3A, right side). This result indicated that the agglomeration phenomenon was significantly reduced after the Fu

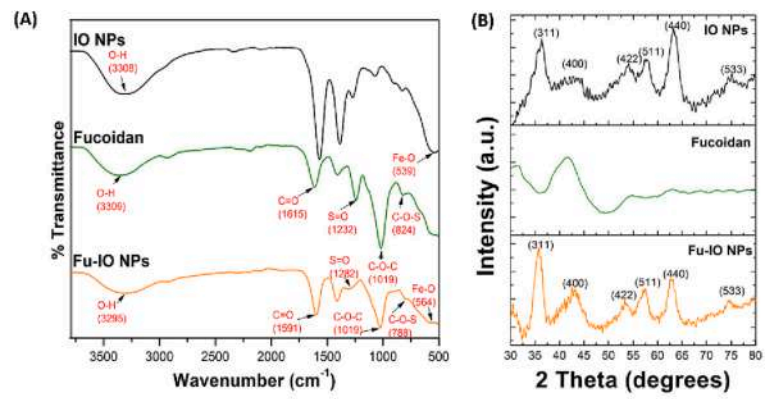

(C)

Element	Mass Norm. (%)	Atom (%)
Iron	72.22	42.69
Oxygen	22.78	57.31
Sum	**100**	**100**

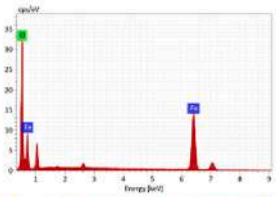

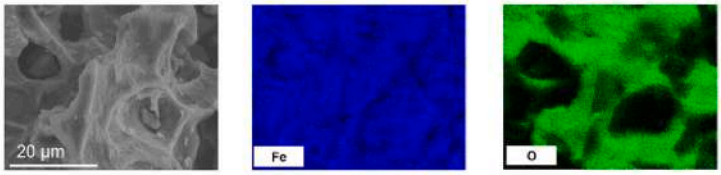

(D)

Element	Mass Norm. (%)	Atom (%)
Iron	48.78	19.35
Oxygen	21.00	29.08
Carbon	23.29	42.96
Nitrogen	4.29	6.78
Sulfur	2.64	1.82
Sum	**100**	**100**

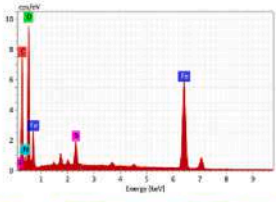

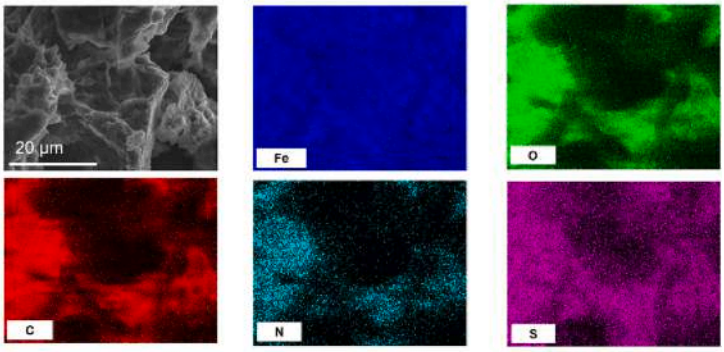

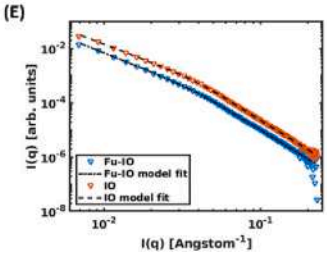

Fig. 1. Structural characteristic studies. (A) Fourier-transform infrared spectroscopy (FTIR) spectrum. (B) X-ray powder diffraction (XRD) pattern of iron oxide nanoparticles (IO NPs), fucoidan (Fu), and Fu-IO NPs. EDX element analysis, SEM image, and chemical composition mapping of (C) IO NPs and (D) Fu-IO NPs. (E) SAXS results of IO NPs and Fu-IO NPs. SAXS data showed similarities between the Fu-IO and IO NPs. The scattering is characterized by two power laws, one at low q revealing the mass fractal and a second at higher q showing the surface fractal of the primary NPs.

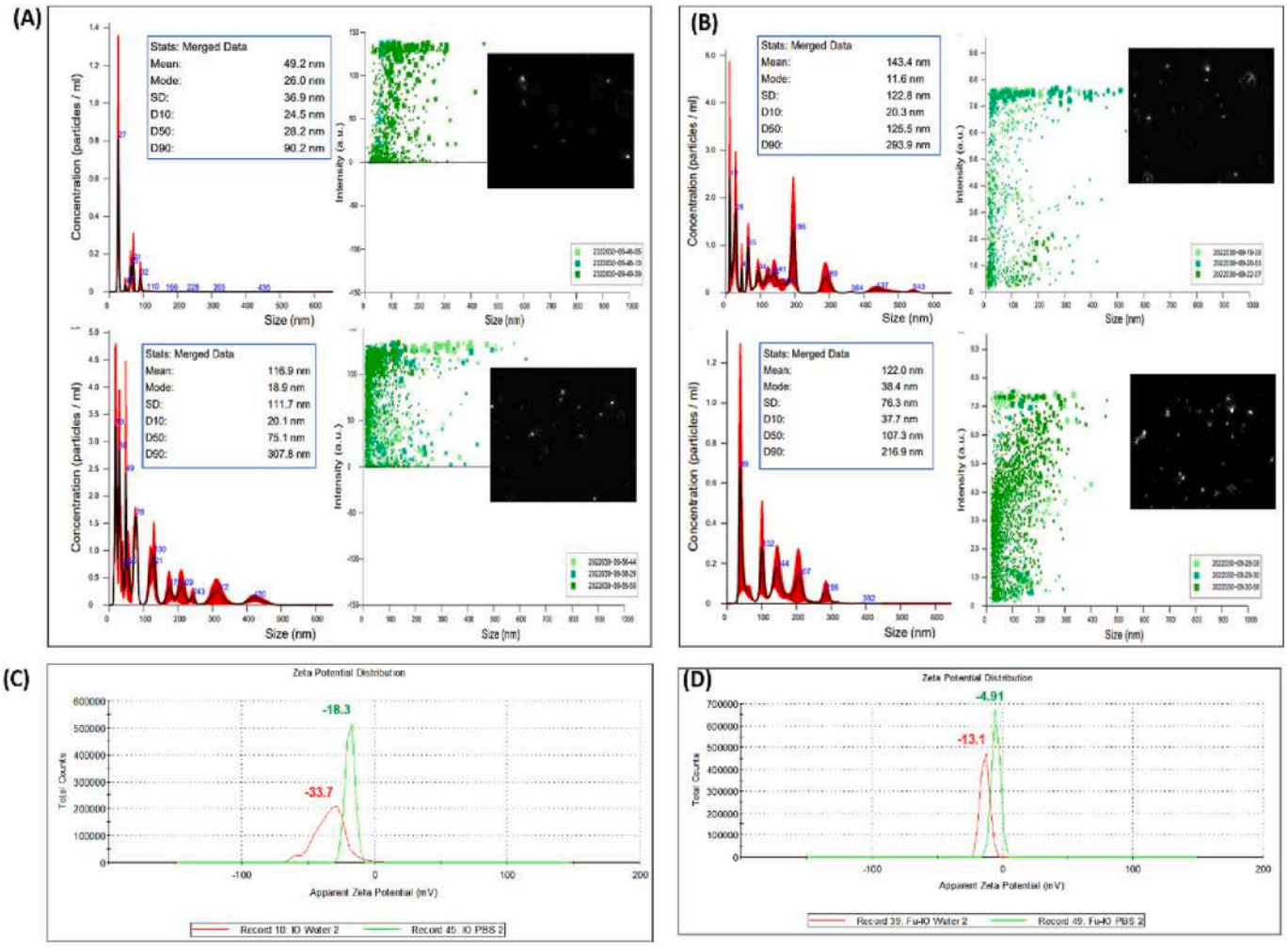

Fig. 2. Size and surface charge distribution profile of the prepared nanoparticles (NPs). Particle size distribution vs. the NP concentration and intensity of (A) iron oxide (IO) NPs and (B) fucoidan (Fu)-IO NPs in water (upper) and phosphate-buffered saline (PBS) (lower) obtained by an NP tracking analysis (NTA). Zeta potentials of (C) IO NPs and (D) Fu-IO NPs in water and in PBS were determined by the Zetasize Nano Series.

coating was added, because of a decline in hydrophobic/magnetic interactions among the IO NPs. We calculated the thickness of Fu in the Fu-IO NPs using ImageJ software [39]. The calculated thickness of Fu-IO NPs was ca. 2.5 nm.

To further evaluate the stabilities of the prepared NPs (IO NPs, and Fu-IO NPs), colloids were observed for 7 days at room temperature. As predicted, the colloidal Fu-IO NPs were more stable than were the IO NPs. From captured images in Fig. 3B, it is evident that the color of IO NPs gradually lightened due to their tendency to aggregate. The NPs sank to the bottom of the cuvette, whereas no change was observed in the colloidal Fu-IO NPs. These data were consistent with the TEM images. Moreover, the size and zeta potential of IO NPs and Fu-IO NPs in water were measured on day 1 and day 7 to confirm the NPs' stabilities. The particle size of prepared NPs increased after 7 days, as shown in Fig. 3C. IO NPs' average nanoparticle size rose dramatically to 110 nm, while Fu-IO NPs' average nanoparticle size increased by 50 nm. In addition, the changes in the zeta potential of Fu-IO NPs were less than that of IO NPs after 7 days. The results indicate an improvement in the stability of IO NPs using encapsulation with Fu shells. The obtained is consistent with previous research [14,40–42].

3.2. *In vitro cellular uptake of the nanoformulations*

Visual TEM and Prussian blue staining were used to confirm whether the NPs had been adsorbed onto the cell surface or the prepared NPs had been internalized/taken up intracellularly. A549 cells without treatment were used as a control group. TEM images clearly demonstrated the process of the trapped Fu-IO NPs after 6 h, 8 h, 12 h, and 24 h of incubation (Fig. 4A). After 6 h of incubation, Fu-IO NPs gradually located around the cells and trafficked into the cells were observed. Then, the number of NPs pervaded intracellularly in organelles such as endosomes/lysosomes increased following the time of incubation. In addition, the destruction of cell membranes and cellular organelles such as mitochondria was observed in A549 cells. Similarly, damaged phenomena were reported in previous studies using Fu alone and when combined with other materials of IO NPs [41,43,44]. Moreover, to evaluate targeted Fu in lung cancer cells, IO NP- and Fu-IO NP-treated A549 cells were stained with Prussian blue at different time points. The prepared NPs were detected inside cells with 6 h of incubation (see Fig. 4B). According to the presence of a blue color, A549 cells had taken up a significantly higher amount of Fu-IO NPs than IO NPs. The number of prepared NPs internalized inside of A549 cells remarkably increased depending on the incubation time. These results indicated that the targeted Fu-IO NPs could quickly be taken up by A549 cells and caused damage to cancer cells owing to the overexpression of P-selectin by A549 cells (which was proven below).

Acting as an MRI contrast agent is a powerful and key property of the IO nanoplatform. To investigate the efficiency of Fu-IO NPs as MRI contrast agents, T2*-weighted MR images of prepared NP-treated HEL 299 and A549 cells were taken using a 7 T PharmaScan (Bruker)

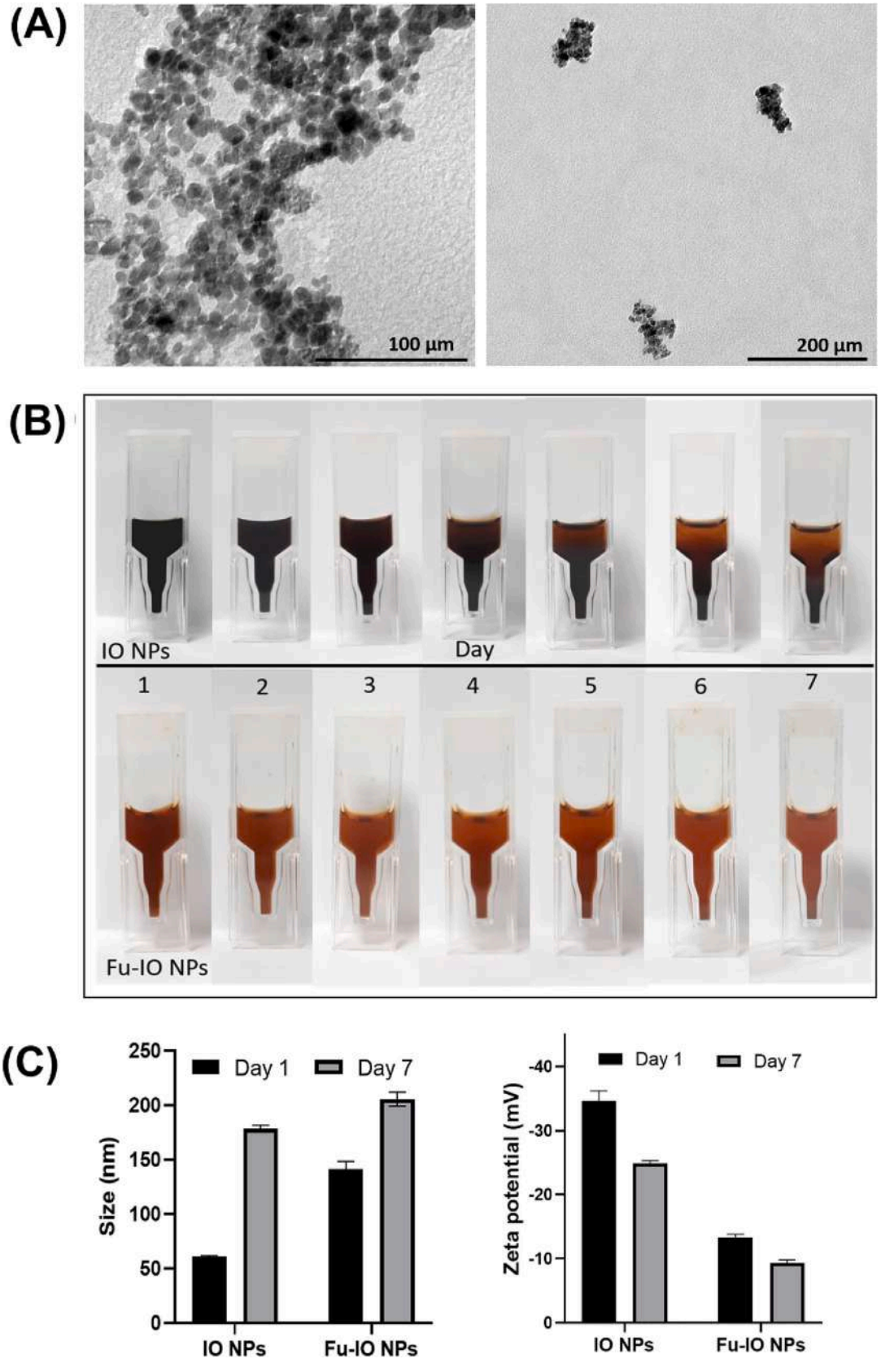

Fig. 3. Morphology and physical properties. (A) TEM images of iron oxide nanoparticles (IO NPs, left side) and fucoidan (Fu)-IO NPs (right side). (B) Photographic data for the stability test of IO NPs and Fu-IO NPs during 1 week at room temperature. (C) Particle size and zeta potential of IO NPs and Fu-IO NPs in water at day 1 and day 7.

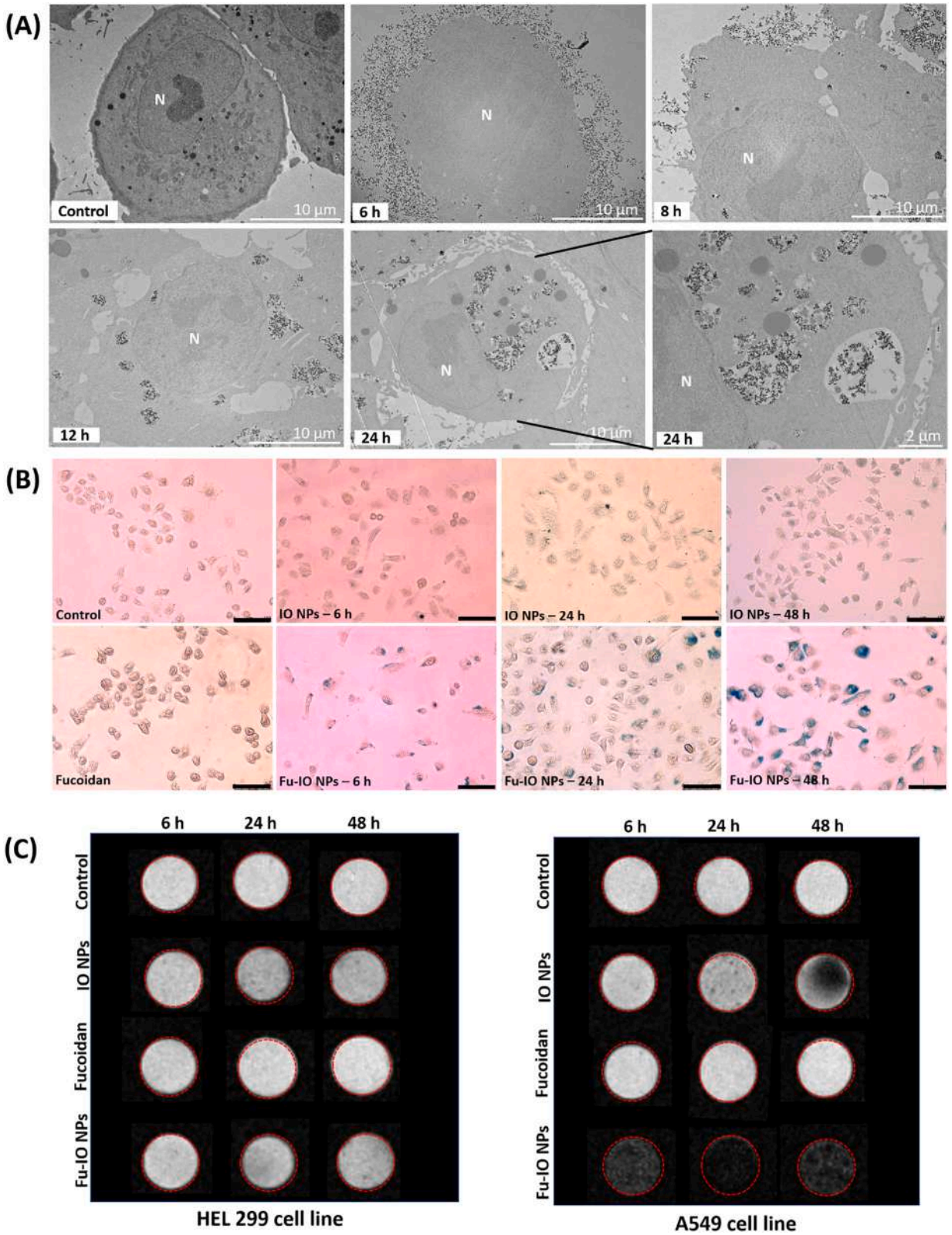

Fig. 4. In vitro cellular uptake experiments. (A) TEM images of cellular internalization of fucoidan-iron oxide nanoparticles (Fu-IO NPs) in the A549 cell line after 6 h, 8 h, 12 h, and 24 h of incubation. (B) Prussian blue staining of A549 cells after 6, 24, and 48 h of incubation with fresh medium, IO NPs (100 μg/mL), Fu (15 μg/mL), and Fu-IO NPs (equivalent to 100 μg/mL IO NPs and 15 μg/mL Fu), (scale bar = 100 μm). (C) MR images of HEL 299 (left) and A549 cells (right) after 6, 24, and 48 h of incubation with IO NPs (100 μg/mL), Fu (15 μg/mL), and Fu-IO NPs (equivalent to 100 μg/mL IO NPs and 15 μg/mL Fu). N, cell nuclei.

(Fig. 4C). The resulting signal intensities showed that the control groups, consisting of cells only, and the Fu groups yielded no difference in signals, while signal intensities of the IO NP and Fu-IO NP groups were gradually reduced following different incubation times, especially in the A549 cell line. Moreover, detailed observations of the intensity of the 1/T2* signal indicated a darkening effect of the Fu-IO NP groups which was clearly visible compared to the IO NP groups. This demonstrated a darkening effect of cells which was dependent on the amount of IO NPs trapped, and was consistent with Prussian blue staining data. These results also proved the Fu-IO NPs' diagnostic capacity to work as MRI contrast agents without interference from the Fu-coated surface. Meanwhile, it was interesting that the Fu-IO NP-treated cancer cells had higher cellular accumulation/interactions compared to Fu-IO NP-treated normal cells, according to visual TEM and Prussian blue staining data. It was thus worth further biochemically analyzing the underlying detailed and potential cellular mechanisms.

3.3. Overexpression of P-selectin and enhanced ROS stress and GSH depletion in A549 cells

P-Selectin or CD62P, which may aid cancer cell invasion of the bloodstream during metastasis, has recently arisen as a therapeutic target for delivering drugs to tumor locations [45]. To clarify the presence of P-selectin in cancer cells, HEL 299 and A549 cells were cultured with an anti-P-selectin/CD62P antibody conjugated with PE. Fluorescence data in Fig. 5A indicate that the expression of P-selectin in A549 lung cancer cells was considerably more significant than that in healthy HEL 299 lung fibroblast cells. In a 2016 study, Shamay et al. found abundant P-selectin expression in lung tumor tissues from 420 clinical samples [45]. In addition, P-selectin can bind to oligosaccharide ligands containing fucoses, such as Fu, heparin, and dextran sulfate. Bachelet et al. proved that Fu has a great affinity for P-selectin and prevented the highest of P-selectin binding to sialyl Lewis X (higher than 20- and 1250-fold compared to heparin and dextran sulfate, respectively) [15]. Therefore, the targeted P-selectin mechanism implies that Fu-based NPs facilitate binding to lung cancer cells compared to healthy cells.

The high level of ROS in cells causes damage to the mitochondrial ultrastructure and depolarizes the MMP resulting in dead cells [11]. So, nanomaterials that can precisely increase cancer intracellular ROS levels are considered potential candidates for application to cancer treatment [46]. Many studies proved the capacity of IO NPs and Fu to induce oxidative stress. IO NPs escalate intracellular ROS stress via the Fenton reaction by releasing ferrous (Fe^{2+}) or ferric (Fe^{3+}) in acidic lysosomes [47,48]. Fu increases ROS levels in lung cancer cells via the knockdown of Toll-like receptor 4 (TLR4) [49]. However, previous findings reported that cancer cells have ROS-shielding mechanisms [4,6], mainly regarding GSH (1– 10 mM within tumor cells) [7,8]. Lately, Fu has attracted the attention of scientists in multidisciplinary arenas including biomaterials, nanomedicine, and anticancer [10,11]. Fu is a biocompatible, sulfated polysaccharide and can be used in nanoformulations with hydrophobic therapeutic agents to increase their colloidal stability [14]. Developing Fu-based targeted delivery cargoes can reduce chemo drug side effects and improve active targeting and delivery efficacy toward P-selectin-overexpressing cancer cells [15–17]. Fu-induced cancer cell death and anti-metastasis are associated with GSH depletion, high cellular ROS levels accumulate, and accompanying damage to mitochondrial structures, caspase bioactivation, and depolarization of the MMP [11].

After co-incubation with NPs, the intracellular ROS production by HEL 299 and A549 cells was examined using fluorescence microscopy. As shown in Fig. 5B, no or less green DCF fluorescence was observed in HEL 299 cells at all time points, indicating the lack of prepared NP-cell interactions in normal cells for sufficient ROS therapies (FU plus CDT). Meanwhile, stronger fluorescence of ROS levels was detected in treated A549 cells (Fig. 5C). However, fluorescence intensities remarkably increased only after 24 h of incubation, indicating that an appropriate time is required for NP-cell interactions to achieve high efficiency. In addition, the achieved cellular ROS levels in A549 cells were the highest in the Fu-IO NP group. Moreover, regarding material characterization, the ROS generation of prepared NPs was verified using TMB [50], as shown in Fig. S2. Herein, Fe^{3+} was transformed to Fe^{2+}, triggering an in-situ Fenton reaction with TMB-supplied H_2O_2 to generate OH radicals, resulting in the TMB-involved chromogenic reaction. Results showed that after 6 h of incubation, the peak absorbance of IO NPs was ca. 3 times higher than that of PBS (Fig. S2). However, the mechanism of Fu-induced ROS production is still unclear. Previous research demonstrated that Fu could induce intracellular ROS production, inhibit cell viability and proliferation, and induce apoptosis in cancer cells [19,49,51]. For example, Wei et al. showed that after 48 h of treatment with 100 μg/mL Fu, intracellular ROS level increased approximately 1.5-fold, with the apoptotic rate of SKM-1 cells increasing to 28.2 % versus 16.4 % in the control group [51]. A study by Zhang and co-workers indicated that after being treated with Fu at 820 μg/mL, levels of intracellular ROS increased which was a contributing factor causing mitochondrial membrane dysfunction and apoptosis of MCF-7 cell lines [19]. As shown in Fig. S2, the absorbance of Fu was about 2-fold higher compared to the PBS control group. Moreover, the intensities of the absorbance of Fu-IO NPs were highest, reaching around 3.5-fold compared to the PBS group. These results suggested that intracellular ROS production was synergistically enhanced, which was attributed to combined chemotherapy (Fu) and chemodynamic theranostics (IO).

In addition, intracellular excess GSH in cancer cells can scavenge ROS produced, limiting the efficacy of ROS treatment [52]. Combining chemodynamic therapy (CDT) and reactive oxygen species (ROS)-boosting strategies referred to in studies as endogenous synergies, has recently been widely developed to reduce GSH levels while generating ROS [4,6]. Furthermore, the study of Jin et al. discovered that Fu reduces intracellular glutathione (GSH) levels by activating ERK1/2 and JNK [53]. The GSH deleption assay, thus, was performed to evaluate the effect of prepared NPs on intracellular GSH level in A549 cells (Fig. 5D). The results revealed that the GSH signal remained nearly constant throughout the control groups. However, the green signal was reduced in IO NPs, Fu, and Fu-IO NPs groups. This indicates that the GSH is consumed by the prepared NPs. Especially the green signal seems totally depleted in A495 cells after 48 h treated with Fu-IO NPs. The previous study showed that GSH levels in JB6 P+ cells were decreased after exposing superparamagnetic iron oxide (SPION) [54]. Besides, fucoidan-decreased intracellular GSH level induces apoptosis via ERK1/2 and JNK activation [53]. As a result, when Fu and IO NPs were combined, the effect of GSH depletion was enhanced (as shown in Fig. 5D).

3.4. Cytotoxicity and inhibition of migration and invasion of lung cancer cells by Fu-IO NPs

Aside from diagnostic applications, IO NPs are a very attractive and viable cancer treatment candidate due to their unique features. *Khan* et al. discovered that IO NPs triggered ROS and autophagy, which resulted in mitochondrial collapse and cell death [43]. Similarly, there are numerous publications on the toxicity of bare IO NPs in cancer cells due to ROS production [29,47,48,55]. Furthermore, the toxicity of IO NPs toward cancer cells was significantly increased by combination therapy (IO NPs plus chemotherapeutic drugs or hyperthermic agents), in which they serve as a reservoir for the regulated release of therapeutic drugs mediated by the intracellular acidic pH [42,50,56]. For example, Wang et al. loaded Fe^{3+} into a depot that responded to the thermal and tumor microenvironment of colorectal tumors, resulting in improved chemodynamic therapy for colorectal tumors [50]. As a result, increasing numbers of differently modified iron-based NPs are being explored as possible anticancer treatment agents.

It is well known that both IO NPs and Fu cause loss of cell viability in a dose- and time-dependent manners [11,57,58]. Herein, to determine

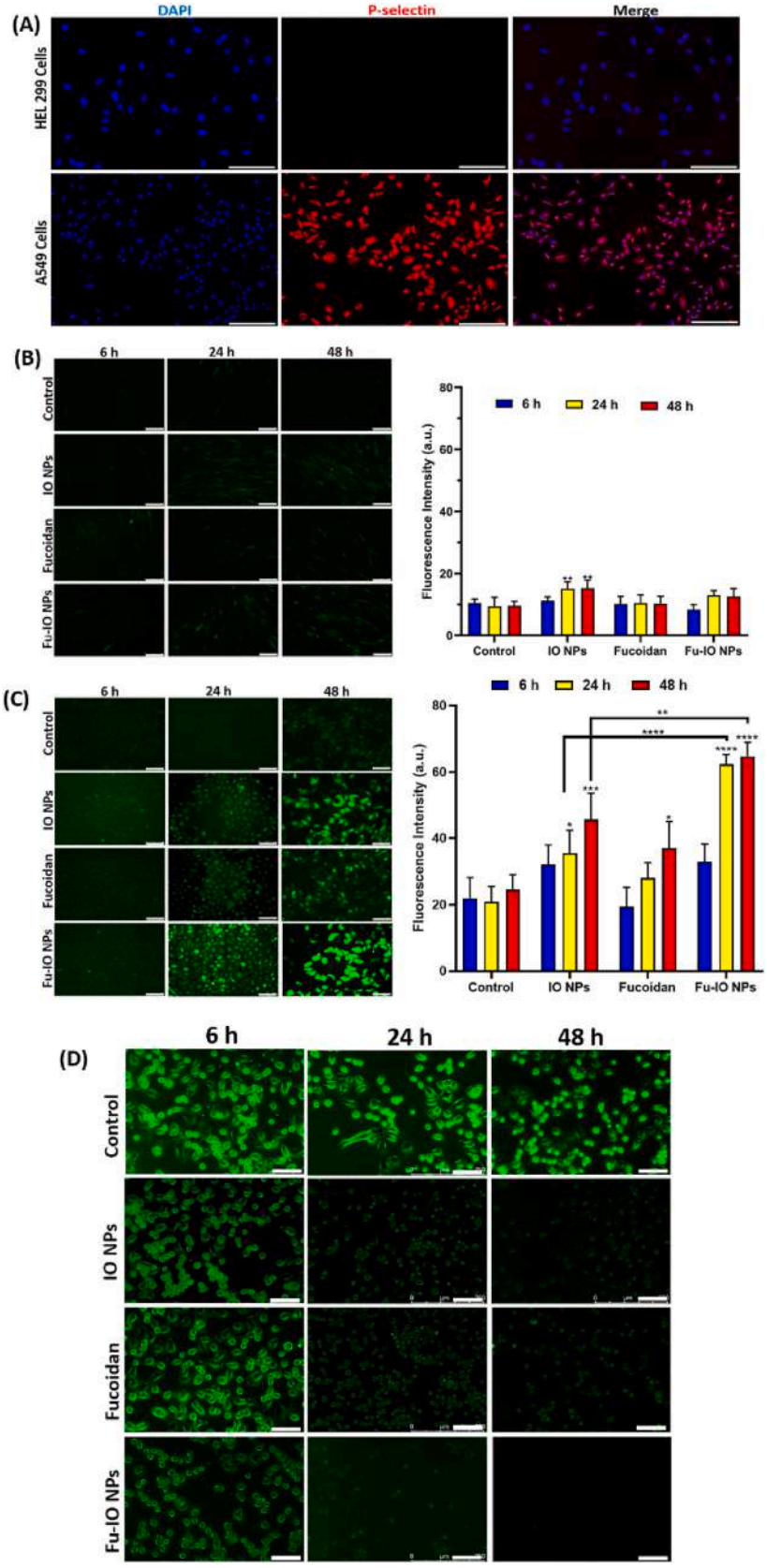

Fig. 5. (A) Representative images of anti-P-selectin protein expression by HEL 299 (upper) and A549 cells (lower) (scale bar = 250 μm). Detection of generated reactive oxygen species (ROS) in treated cells after at 6, 24, and 48 h of incubation with fresh medium, iron oxide nanoparticles (IO NPs) (100 μg/mL), fucoidan (Fu) (15 μg/mL), and Fu-IO NPs (equivalent to 100 μg/mL IO NPs and 15 μg/mL Fu). Representative images and ROS generation by the fluorescence intensity of (B) HEL 299 and (C) A549 cells stained with DCFH-DA and the generated cellular DCF fluorescent signals as determined by fluorescence microscopy (scale bar = 100 μm), (* $p < 0.05$, ** $p < 0.01$, *** $p < 0.001$, **** $p < 0.0001$) (compared to control). (D) Green fluorescence indicates GSH levels in A549 cells stained by 5-chloromethylfluorescein diacetate (CMFDA) fluorescent dye (scale bar = 100 μm).

the ideal concentration and time treatment of NPs that would not affect normal cells, a cytotoxicity assay was performed on HEL 299 cells (normal healthy lung fibroblasts) with a series of IO-based concentrations of Fu-IO NPs (0– 500 μg/mL) at different time points. Fig. 6A shows that after 6 and 24 h of incubation with Fu-IO NPs, cell viabilities exhibited no obvious cytotoxicity with the control group containing fresh media even at 500 μg/mL. After 48 h of incubation, the cell viability was slightly reduced at 200 and 500 μg/mL. Therefore, the 100 μg/mL IO-based concentration of Fu-IO NPs was biocompatible and was used for further experiments with minimal cytotoxicity toward normal cells without unwanted side effects.

The tetrazolium dye, MTT, is easily transformed to formazan by mitochondrial succinate dehydrogenase in viable cells. We performed an MTT assay in order to evaluate the cytotoxicity of the prepared NPs to A549 cancer cells. Here, concentrations of IO NPs (100 μg/mL) and Fu (15 μg/mL) were used, which were equivalent to the contents of IO NPs and Fu inside the working Fu-IO NPs calculated based on a colorimetric assay. As shown in Fig. 6B, the viability of A549 cells decreased by <80 % after 48 h of co-incubation with IO NPs and Fu alone. Meanwhile, with only 6 h of co-incubation with Fu-IO NPs, cell viability was reduced by <80 %. Following 24 and 48 h of Fu-IO NP treatment, survival of cells remarkably dropped to <70 % and 50 %, respectively. This indicated precise synergistic toxicity using the combination of chemotherapy-CDT with time-dependent antiproliferative activity. The synergistic effect of the Fu-IO NPs was further confirmed by live/dead double staining [59]. After 48 h of treatment with Fu-IO NPs, cells were stained with a Live and Dead Assay Kit (live cells in green and dead cells in red). As shown in Fig. 6C, the fluorescent results of the live/dead assay were consistent with those of the MTT assay results.

Migration and invasion processes play essential during cancer metastasis [60,61]. So, migration and invasion of cells are considered a measure of the metastatic ability of cancer cells. A previous study found that Fu inhibits the migration and invasion of lung cancer cells (A549 cell line), leading to an anti-metastatic effect via extracellular signal-regulated kinase 1/2 and Akt-mammalian target of rapamycin (mTOR) downregulation [31], and inhibition of the transforming growth factor receptor (TGFR)/Smad7/Smurf2-dependent pathway [62]. So, in this study, we performed a scratch-wound assay to determine the migration inhibition ability of the prepared NPs in A549 cells. As shown in Fig. 7A, after 48 h of co-incubation with Fu-IO NPs, A549 cell migration was

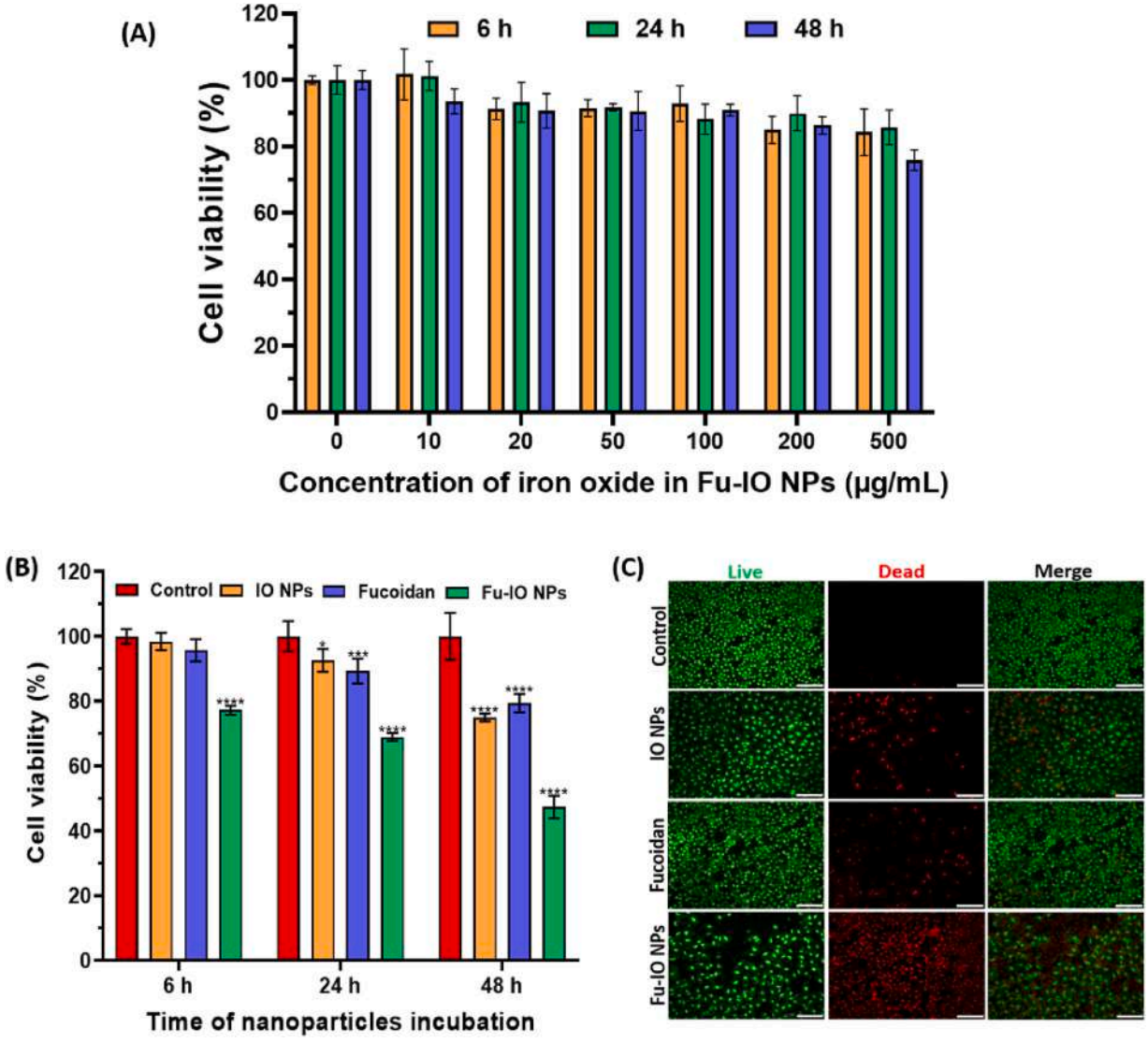

Fig. 6. (A) Cell viability of HEL 299 cells after 6, 24, and 48 h of incubation with different iron oxide (IO)-based concentrations in fucoidan (Fu)-IO nanoparticles (NPs). Error bars represent the mean ± SD ($n = 3$). (B) MTT analysis of IO NPs (100 μg/mL), Fu (15 μg/mL), and Fu-IO NPs (equivalent to 100 μg/mL IO NPs and 15 μg/mL Fu) treated A549 cells at 6, 24, and 48 h. Error bars represent the mean ± SD ($n = 4$), * $p < 0.05$, *** $p < 0.001$, **** $p < 0.0001$. (compared to control group) (C) Representative live/dead staining images of A549 cells after 48 h of incubation with IO NPs, Fu, and Fu-IO NPs, (scale bar = 100 μm).

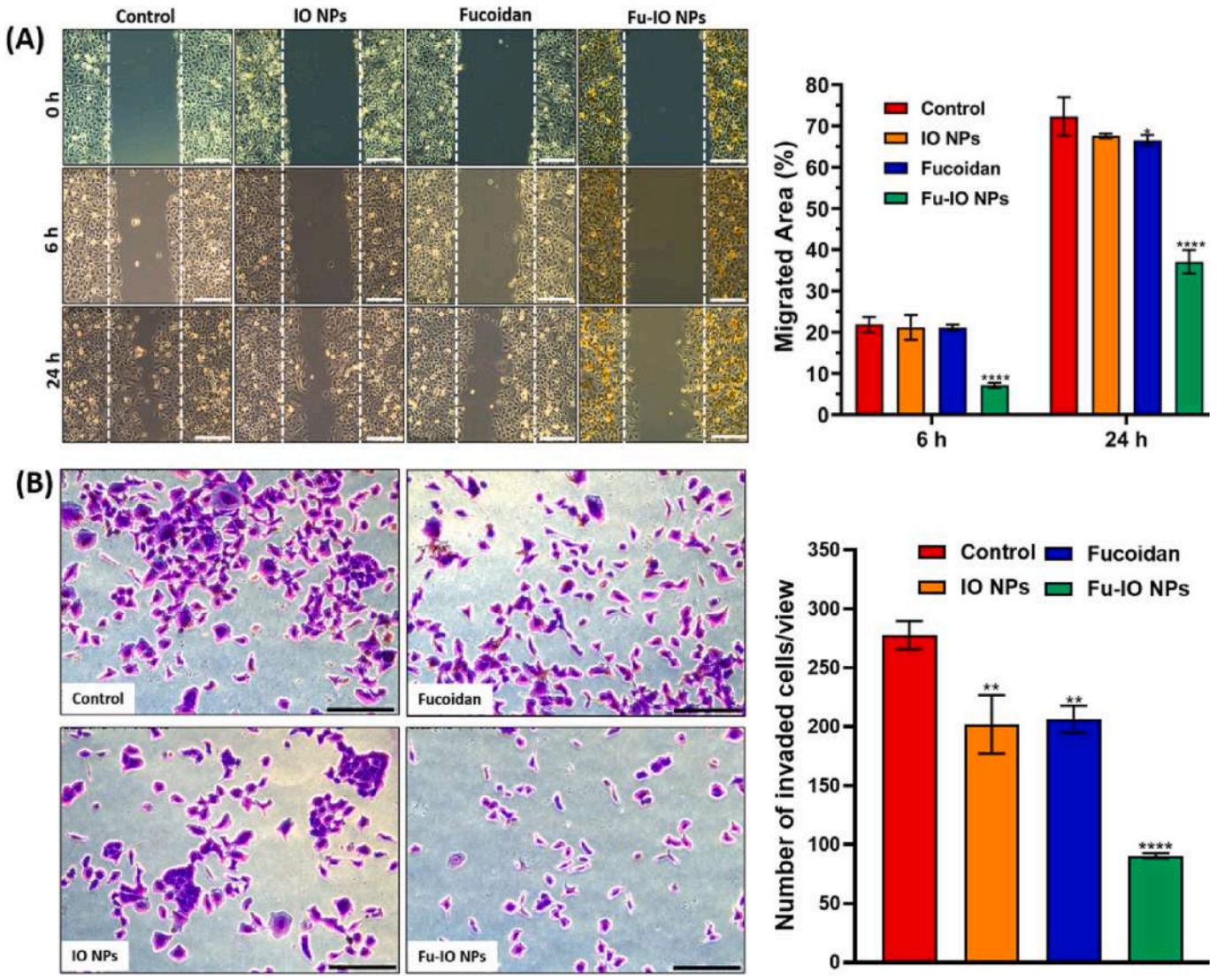

Fig. 7. Inhibitory activities of the control, iron oxide (IO) nanoparticle (NP; 100 μg/mL), fucoidan (Fu; 15 μg/mL), and Fu-IO NP (equivalent to 100 μg/mL IO NPs and 15 μg/mL Fu) groups against the migration and invasion abilities of A549 cells using (A) a scratch-wound assay and (B) transwell invasion assay. Scale bar = 250 μm, * $p < 0.05$, ** $p < 0.01$, **** $p < 0.0001$. (compared to control group).

significantly suppressed by up to ca. 15 % and 35 % at 6 and 24 h, respectively. Meanwhile, migrated areas of the IO NP and Fu groups had no or less significant differences compared to the control group. These results again indicated that the synergistic effect of the Fu-IO NPs significantly inhibited the migration of A549 cells. Moreover, to investigate the effect of the prepared NPs on cell anti-invasion, a transwell invasion assay was performed with A549 cells. As illustrated in Fig. 7B, the number of invaded cells was slightly reduced in the IO NP and Fu groups, while Fu-IO NPs inhibited up to 50 % of the number of A549 cells that invaded, compared to control group. These results highlighted that Fu-IO NPs could strongly inhibit invasion by A549 cells, which was consistent with the in vitro scratch-wound assay results. Similarly, a previous study showed that using a combination of Fu and other agents more highly inhibited the migration and invasion of A549 cells only Fu [62].

The antitumor effect of chemotherapy plus chemodynamic therapy in the mouse A549 tumor-bearing model was evaluated by measuring tumor volume. We found that no obvious inhibition of tumor growth was observed in saline control group (Fig. 8A). Compared to control group, Fu or IO group had a partial inhibitory effect possibly due to the monotherapy capability from chemotherapy or chemodynamic therapy. Moreover, Fu-IO NP mediated combination treatment of chemotherapy and chemodynamic therapy showed the most potent antitumor efficacy and almost no tumor recurred in the treated mice until 14 d thereafter. Moreover, the specific in vivo tumor accumulation of Fu-IO NPs resulted in increased oxidative stress compared to that of group of untreated control, tumor received Fu, and tumor received IO, which was attributed to effects of chemodynamic therapeutic IO plus chemotherapeutic Fu (Fig. 8B and C), which effectively killed the tumor cells. As shown in Fig. 8D, compared to the untreated tumor group, the group with tumors given Fu-IO NP had great dark contrast effects on T2 MRI due to their superparamagnetic properties. Owing to the high expression of P-selectin in lung tumors, the administered Fu-IO NPs possessed the capability of long-term accumulation in lung tumors according to the microscopic data of in vivo Prussian blue staining (visual blue color) suggesting great iron deposition in the tumor region (Fig. 8E), consistent with the in vitro results (Fig. 4). In our in vivo studies, we observed histological changes in major tissues, including the heart, liver, spleen, lungs, and kidneys, as well as tumors by H&E staining (Fig. 8F). Findings of H&E staining evidenced that there was no obvious damage to tissues of experimental mice. An in vivo safety assessment for tumor-bearing mice proved that Fu-IO NP had no significant systemic toxicity toward

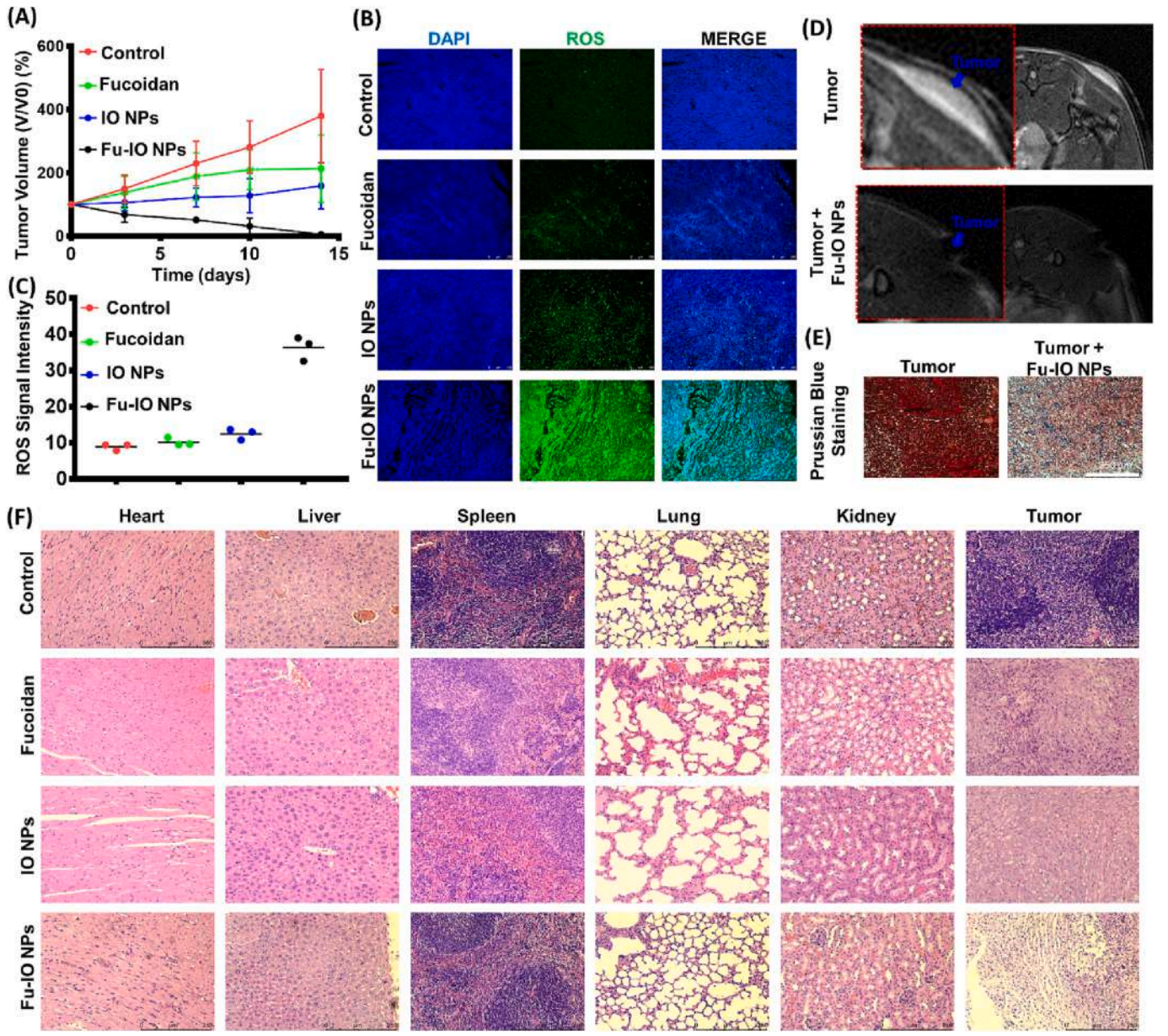

Fig. 8. In vivo (A) Antitumor efficacy, (B) qualitative and (C) quantitative cellular ROS DCFDA, (D) MRI, (E) Prussian blue, and (F) H&E assays. The in vivo data indicated that the fucoidan-iron oxide nanoparticles (Fu-IO NPs) were biocompatible, were able to accumulate in lung tumors, caused tumor oxidative stress, and were diagnosable by MRI. (Scale bar: 250 μm).

mice.

4. Conclusions

Chemodynamic therapeutic agents for lung cancer are usually compromised by insufficient colloidal stability, low production of ROS, and low target efficiency. Herein, nano-formulated IO with Fu as a lung cancer cell-targeted moiety (Fu-IO NPs) was constructed to overcome these issues and achieve remote MRI-diagnosable in lung cancer cells. Remote monitoring of non-invasive MRI data showed that Fu-IO NPs could precisely target cancer cells and enhance the MRI contrast efficacy. As expected, Fu-IO NPs efficiently accumulated in lung cancer cells compared to normal healthy cells, thus enhancing their anticancer efficacy. Moreover, biocompatible Fu-IO NPs produced excess cellular ROS inside lung cancer cells through the Fenton reaction of IO and the biological effects of Fu, which effectively inhibited the proliferation and metastasis of lung cancer cells. These biochemical results suggested that the nanoscale ROS generator Fu-IO NPs could be applied in MRI-diagnosable lung cancer theranostics by synergizing chemotherapy-CDT. Therefore, using Fu-IO NPs, a strategy of multimodal anticancer therapeutics as endogenous synergistic agents for CDT, would help enhance anticancer efficacies in the future.

Declaration of competing interest

All authors declare that no conflicts of interest exist.

Acknowledgments

This study was financially supported by grants from the National Science and Technology Council (NSTC), Taiwan (111-2320-B-038-039-).

Appendix A. Supplementary data

Supplementary data to this article can be found online at https://doi.org/10.1016/j.ijbiomac.2023.123821.

References

[1] X. Xu, Z. Zeng, J. Chen, B. Huang, Z. Guan, Y. Huang, Z. Huang, C. Zhao, Tumor-targeted supramolecular catalytic nanoreactor for synergistic chemo/chemodynamic therapy via oxidative stress amplification and cascaded Fenton reaction, Chem. Eng. J. 390 (2020), 124628.

[2] L. Liang, L. Wen, Y. Weng, J. Song, H. Li, Y. Zhang, X. He, W. Zhao, M. Zhan, Y. Li, L. Lu, Y. Xin, C. Lu, Homologous-targeted and tumor microenvironment-activated hydroxyl radical nanogenerator for enhanced chemoimmunotherapy of non-small cell lung cancer, Chem. Eng. J. 425 (2021), 131451.

[3] E.D. Quiñones, T.-Y. Lu, K.-T. Liu, Y.-J. Fan, E.-Y. Chuang, J. Yu, Glycol chitosan/iron oxide/polypyrrole nanoclusters for precise chemodynamic/photothermal synergistic therapy, Int. J. Biol. Macromol. 203 (2022) 268–279.

[4] Q. Sun, B. Liu, Z. Wang, L. Feng, R. Zhao, S. Dong, Y. Dong, L. Zhong, S. Gai, P. Yang, H2O2/O2 self-supplementing and GSH-depleting Ca2+ nanogenerator with hyperthermia-triggered, TME-responsive capacities for combination cancer therapy, Chem. Eng. J. 425 (2021), 131485.

[5] P. Zhao, Z. Tang, X. Chen, Z. He, X. He, M. Zhang, Y. Liu, D. Ren, K. Zhao, W. Bu, Ferrous-cysteine–phosphotungstate nanoagent with neutral pH Fenton reaction activity for enhanced cancer chemodynamic therapy, Mater. Horiz. 6 (2) (2019) 369–374.

[6] J.-S. Lan, L. Liu, R.-F. Zeng, Y.-H. Qin, J.-W. Hou, S.-S. Xie, S. Yue, J. Yang, R.J. Y. Ho, Y. Ding, T. Zhang, Tumor-specific carrier-free nanodrugs with GSH depletion and enhanced ROS generation for endogenous synergistic anti-tumor by a chemotherapy-photodynamic therapy, Chem. Eng. J. 407 (2021), 127212.

[7] Y. Liu, J. Wu, Y. Jin, W. Zhen, Y. Wang, L. Jianhua, L. Jin, S. Zhang, Y. Zhao, S. Song, Y. Yang, H. Zhang, Copper(I) phosphide nanocrystals for in situ self-generation magnetic resonance imaging-guided photothermal-enhanced chemodynamic synergetic therapy resisting deep-seated tumor, Adv. Funct. Mater. 29 (2019), 1904678.

[8] X. Jia, J. He, L. Shen, J. Chen, Z. Wei, X. Qin, D. Niu, Y. Li, J. Shi, Gradient redox-responsive and two-stage rocket-mimetic drug delivery system for improved tumor accumulation and safe chemotherapy, Nano Lett. 19 (12) (2019) 8690–8700.

[9] W. Lin, H. Liu, L. Chen, J.-X. Chen, Z. Dong, Q. Cheng, F. Yang, Q. Zeng, T. Chen, Pre-clinical MRI-guided intravesical instillation theranosis of bladder cancer by tumor-selective oxygen nanogenerator, Nano Today 38 (2021), 101124.

[10] C. Oliveira, N.M. Neves, R.L. Reis, A. Martins, T.H. Silva, A review on fucoidan antitumor strategies: from a biological active agent to a structural component of fucoidan-based systems, Carbohydr. Polym. 239 (2020), 116131.

[11] Y. Lin, X. Qi, H. Liu, K. Xue, S. Xu, Z. Tian, The anti-cancer effects of fucoidan: a review of both in vivo and in vitro investigations, Cancer Cell Int. 20 (2020) 154.

[12] K.Y. Lu, P.R. Jheng, L.S. Lu, L. Rethi, F.L. Mi, E.Y. Chuang, Enhanced anticancer effect of ROS-boosted photothermal therapy by using fucoidan-coated polypyrrole nanoparticles, Int. J. Biol. Macromol. 166 (2021) 98–107.

[13] T.M. Don, W.J. Chang, P.R. Jheng, Y.C. Huang, E.Y. Chuang, Curcumin-laden dual-targeting fucoidan/chitosan nanocarriers for inhibiting brain inflammation via intranasal delivery, Int. J. Biol. Macromol. 181 (2021) 835–846.

[14] E.D. Obluchinskaya, O.N. Pozharitskaya, E.V. Flisyuk, A.N. Shikov, Formulation, optimization and in vivo evaluation of fucoidan-based cream with anti-inflammatory properties, Mar. Drugs 19 (11) (2021).

[15] L. Bachelet, I. Bertholon, D. Lavigne, R. Vassy, M. Jandrot-Perrus, F. Chaubet, D. Letourneur, Affinity of low molecular weight fucoidan for P-selectin triggers its binding to activated human platelets, Biochim. Biophys. Acta 1790 (2) (2009) 141–146.

[16] M. Jafari, V. Sriram, Z. Xu, G.M. Harris, J.Y. Lee, Fucoidan-doxorubicin nanoparticles targeting P-selectin for effective breast cancer therapy, Carbohydr. Polym. 249 (2020), 116837.

[17] J. Garcia, N. Callewaert, L. Borsig, P-selectin mediates metastatic progression through binding to sulfatides on tumor cells, Glycobiology 17 (2) (2007) 185–196.

[18] L. Yang, P. Wang, H. Wang, Q. Li, H. Teng, Z. Liu, W. Yang, L. Hou, X. Zou, Fucoidan derived from undaria pinnatifida induces apoptosis in human hepatocellular carcinoma SMMC-7721 cells via the ROS-mediated mitochondrial pathway, Mar. Drugs 11 (6) (2013) 1961–1976.

[19] Z. Zhang, K. Teruya, H. Eto, S. Shirahata, Fucoidan extract induces apoptosis in MCF-7 cells via a mechanism involving the ROS-dependent JNK activation and mitochondria-mediated pathways, PLoS One 6 (11) (2011), e27441.

[20] M. Xue, Y. Ge, J. Zhang, Y. Liu, Q. Wang, L. Hou, Z. Zheng, Fucoidan inhibited 4T1 mouse breast cancer cell growth in vivo and in vitro via downregulation of Wnt/β-catenin signaling, Nutr. Cancer 65 (3) (2013) 460–468.

[21] W. Li, D. Xue, M. Xue, J. Zhao, H. Liang, Y. Liu, T. Sun, Fucoidan inhibits epithelial-to-mesenchymal transition via regulation of the HIF-1α pathway in mammary cancer cells under hypoxia, Oncol. Lett. 18 (1) (2019) 330–338.

[22] M. Chu, Y. Shao, J. Peng, X. Dai, H. Li, Q. Wu, D. Shi, Near-infrared laser light mediated cancer therapy by photothermal effect of Fe3O4 magnetic nanoparticles, Biomaterials 34 (16) (2013) 4078–4088.

[23] D. Zhang, J. Wang, Z. Wang, R. Wang, L. Song, T. Zhang, X. Lin, P. Shi, H. Xin, X. Pang, Polyethyleneimine-coated Fe3O4 nanoparticles for efficient siRNA delivery to human mesenchymal stem cells derived from different tissues, Sci. Adv. Mater. 7 (2015).

[24] G. Schneider, G. Decher, From functional core/shell nanoparticles prepared via layer-by-layer deposition to empty nanospheres, Nano Lett. 4 (2004).

[25] D.-G. Liu, C.-H. Chang, L.-C. Chiang, M.-H. Lee, C.-F. Chang, C.-Y. Lin, C.-C. Liang, T.-H. Lee, S.-W. Lin, C.-Y. Liu, C.-S. Hwang, J.-C. Huang, C.-K. Kuan, H.-S. Wang, Y.-C. Liu, F.-H. Tseng, J.-Y. Chuang, W.-R. Liao, H.-C. Li, C.-J. Su, K.-F. Liao, Y.-Q. Yeh, O. Shih, W.-R. Wu, C.-A. Wang, U. Jeng, Optical design and performance of the biological small-angle X-ray scattering beamline at the Taiwan photon source, J. Synchrotron Radiat. 28 (6) (2021) 1954–1965.

[26] O. Shih, K.-F. Liao, Y.-Q. Yeh, C.-J. Su, C.-A. Wang, J.-W. Chang, W.-R. Wu, C.-C. Liang, C.-Y. Lin, T.-H. Lee, C.-H. Chang, L.-C. Chiang, C.-F. Chang, D.-G. Liu, M.-H. Lee, C.-Y. Liu, T.-W. Hsu, B. Mansel, M.-C. Ho, C.-Y. Shu, F. Lee, E. Yen, T.-C. Lin, U. Jeng, Performance of the new biological small- and wide-angle X-ray scattering beamline 13A at the Taiwan photon source, J. Appl. Crystallogr. 55 (2) (2022) 340–352.

[27] J. Kieffer, V. Valls, N. Blanc, C. Hennig, New tools for calibrating diffraction setups, J. Synchrotron Radiat. 27 (Pt 2) (2020) 558–566.

[28] C.S. Chiang, Y.J. Lin, R. Lee, Y.H. Lai, H.W. Cheng, C.H. Hsieh, W.C. Shyu, S. Y. Chen, Combination of fucoidan-based magnetic nanoparticles and immunomodulators enhances tumour-localized immunotherapy, Nat. Nanotechnol. 13 (8) (2018) 746–754.

[29] M. Calero, M. Chiappi, A. Lazaro-Carrillo, M.J. Rodríguez, F.J. Chichón, K. Crosbie-Staunton, A. Prina-Mello, Y. Volkov, A. Villanueva, J.L. Carrascosa, Characterization of interaction of magnetic nanoparticles with breast cancer cells, J. Nanobiotechnol. 13 (2015) 16.

[30] E. Kim, J.M. Kim, L. Kim, S.J. Choi, I.S. Park, J.Y. Han, Y.C. Chu, E.S. Choi, K. Na, S. S. Hong, The effect of neutral-surface iron oxide nanoparticles on cellular uptake and signaling pathways, Int. J. Nanomedicine 11 (2016) 4595–4607.

[31] H. Lee, J.S. Kim, E. Kim, Fucoidan from seaweed Fucus vesiculosus inhibits migration and invasion of human lung cancer cell via PI3K-akt-mTOR pathways, PLoS One 7 (11) (2012), e50624.

[32] S.Che Soh, M.Mohd Yusof, A.Abd Rahman Azmi, M. Shamsuddin, W.F.Wan Nor, Synthesis and physicochemical properties of magnetite nanoparticles (Fe3O4) as potential solid support for homogeneous catalysts, Malays. J. Anal. Sci. 22 (2018) 768–774.

[33] V.A.J. Silva, P.L. Andrade, M.P.C. Silva, D.A. Bustamante, L.De Los Santos Valladares, J.Albino Aguiar, Synthesis and characterization of Fe3O4 nanoparticles coated with fucan polysaccharides, J. Magn. Magn. Mater. 343 (2013) 138–143.

[34] B. Hammouda, A new guinier-porod model, J. Appl. Crystallogr. 43 (4) (2010) 716–719.

[35] T. Li, A.J. Senesi, B. Lee, Small angle X-ray scattering for nanoparticle research, Chem. Rev. 116 (18) (2016) 11128–11180.

[36] D. Bobo, K.J. Robinson, J. Islam, K.J. Thurecht, S.R. Corrie, Nanoparticle-based medicines: a review of FDA-approved materials and clinical trials to date, Pharm. Res. 33 (10) (2016) 2373–2387.

[37] M. Danaei, M. Dehghankhold, S. Ataei, F. Hasanzadeh Davarani, R. Javanmard, A. Dokhani, S. Khorasani, M.R. Mozafari, Impact of particle size and polydispersity index on the clinical applications of lipidic nanocarrier systems, Pharmaceutics 10 (2) (2018).

[38] S. Jeon, J. Clavadetscher, D.K. Lee, S.V. Chankeshwara, M. Bradley, W.S. Cho, Surface charge-dependent cellular uptake of polystyrene nanoparticles, Nanomaterials (Basel) 8 (12) (2018).

[39] D. Al Husseini, J. Zhou, D. Willhelm, T. Hastings, G.S. Day, H.-C. Zhou, G.L. Coté, X. Qian, R. Gutierrez-Osuna, P.T. Lin, S.A. Sukhishvili, All-nanoparticle layer-by-layer coatings for mid-IR on-chip gas sensing, Chem. Commun. 56 (91) (2020) 14283–14286.

[40] Y. Park, H. Cho, Improvement in the dispersion stability of iron oxide nanoparticles in highly concentrated brine solution using encapsulation with polymer-polymer crosslinked shells, Adv. Powder Technol. 31 (12) (2020) 4743–4750.

[41] Q. Feng, Y. Liu, J. Huang, K. Chen, J. Huang, K. Xiao, Uptake, distribution, clearance, and toxicity of iron oxide nanoparticles with different sizes and coatings, Sci. Rep. 8 (1) (2018) 2082.

[42] A. Figuerola, R. Di Corato, L. Manna, T. Pellegrino, From iron oxide nanoparticles towards advanced iron-based inorganic materials designed for biomedical applications, Pharmacol. Res. 62 (2) (2010) 126–143.

[43] M.I. Khan, A. Mohammad, G. Patil, S.A. Naqvi, L.K. Chauhan, I. Ahmad, Induction of ROS, mitochondrial damage and autophagy in lung epithelial cancer cells by iron oxide nanoparticles, Biomaterials 33 (5) (2012) 1477–1488.

[44] D. Gupta, M. Silva, K. Radziun, D.C. Martinez, C.J. Hill, J. Marshall, V. Hearnden, M.A. Puertas-Mejia, G.C. Reilly, Fucoidan inhibition of osteosarcoma cells is species and molecular weight dependent, Mar. Drugs 18 (2) (2020).

[45] Y. Shamay, M. Elkabets, H. Li, J. Shah, S. Brook, F. Wang, K. Adler, E. Baut, M. Scaltriti, P.V. Jena, E.E. Gardner, J.T. Poirier, C.M. Rudin, J. Baselga, A. Haimovitz-Friedman, D.A. Heller, P-selectin is a nanotherapeutic delivery target in the tumor microenvironment, Sci. Transl. Med. 8 (345) (2016), 345ra87.

[46] D.N. Păduraru, D. Ion, A.G. Niculescu, F. Mușat, O. Andronic, A.M. Grumezescu, A. Bolocan, Recent developments in metallic nanomaterials for cancer therapy, diagnosing and imaging applications, Pharmaceutics 14 (2) (2022).

[47] G. Huang, H. Chen, Y. Dong, X. Luo, H. Yu, Z. Moore, E.A. Bey, D.A. Boothman, J. Gao, Superparamagnetic iron oxide nanoparticles: amplifying ROS stress to improve anticancer drug efficacy, Theranostics 3 (2) (2013) 116–126.

[48] S. Wang, J. Luo, Z. Zhang, D. Dong, Y. Shen, Y. Fang, L. Hu, M. Liu, C. Dai, S. Peng, Z. Fang, P. Shang, Iron and magnetic: new research direction of the ferroptosis-based cancer therapy, Am. J. Cancer Res. 8 (10) (2018) 1933–1946.

[49] H.Y. Hsu, T.Y. Lin, M.K. Lu, P.J. Leng, S.M. Tsao, Y.C. Wu, Fucoidan induces toll-like receptor 4-regulated reactive oxygen species and promotes endoplasmic reticulum stress-mediated apoptosis in lung cancer, Sci. Rep. 7 (2017) 44990.
[50] S. Wang, Y. Yang, H. Wu, J. Li, P. Xie, F. Xu, L. Zhou, J. Zhao, H. Chen, Thermosensitive and tum or microenvironment activated nanotheranostics for the chemodynamic/photothermal therapy of colorectal tumor, J. Colloid Interface Sci. 612 (2022) 223–234.
[51] C. Wei, Q. Xiao, X. Kuang, T. Zhang, Z. Yang, Fucoidan inhibits proliferation of the SKM-1 acute myeloid leukaemia cell line via the activation of apoptotic pathways and production of reactive oxygen species, Mol. Med. Rep. 12 (2015).
[52] B. Niu, K. Liao, Y. Zhou, T. Wen, G. Quan, X. Pan, C. Wu, Application of glutathione depletion in cancer therapy: enhanced ROS-based therapy, ferroptosis, and chemotherapy, Biomaterials 277 (2021), 121110.
[53] J.-O. Jin, M.-G. Song, Y.-N. Kim, J.-I. Park, J.-Y. Kwak, The mechanism of fucoidan-induced apoptosis in leukemic cells: involvement of ERK1/2, JNK, glutathione, and nitric oxide, Mol. Carcinog. 49 (8) (2010) 771–782.
[54] A.R. Murray, E. Kisin, A. Inman, S.-H. Young, M. Muhammed, T. Burks, A. Uheida, A. Tkach, M. Waltz, V. Castranova, B. Fadeel, V.E. Kagan, J.E. Riviere, N. Monteiro-Riviere, A.A. Shvedova, Oxidative stress and dermal toxicity of iron oxide nanoparticles in vitro, Cell Biochem. Biophys. 67 (2) (2013) 461–476.
[55] A.A. Hernández-Hernández, G. Aguirre-Álvarez, R. Cariño-Cortés, L.H. Mendoza-Huizar, R. Jiménez-Alvarado, Iron oxide nanoparticles: synthesis, functionalization, and applications in diagnosis and treatment of cancer, Chem. Pap. 74 (11) (2020) 3809–3824.
[56] N.V.S. Vallabani, S. Singh, Recent advances and future prospects of iron oxide nanoparticles in biomedicine and diagnostics, 3Biotech 8 (6) (2018) 279.
[57] C.A. Quinto, P. Mohindra, S. Tong, G. Bao, Multifunctional superparamagnetic iron oxide nanoparticles for combined chemotherapy and hyperthermia cancer treatment, Nanoscale 7 (29) (2015) 12728–12736.
[58] F. Atashrazm, R.M. Lowenthal, G.M. Woods, A.F. Holloway, J.L. Dickinson, Fucoidan and cancer: a multifunctional molecule with anti-tumor potential, Mar. Drugs 13 (4) (2015) 2327–2346.
[59] L. Zhang, G. He, Y. Yu, Y. Zhang, X. Li, S. Wang, Design of Biocompatible Chitosan/Polyaniline/Laponite hydrogel with photothermal conversion capability, Biomolecules 12 (8) (2022) 1089.
[60] F. van Zijl, G. Krupitza, W. Mikulits, Initial steps of metastasis: cell invasion and endothelial transmigration, Mutat. Res. 728 (1–2) (2011) 23–34.
[61] S. Luanpitpong, S.J. Talbott, Y. Rojanasakul, U. Nimmannit, V. Pongrakhananon, L. Wang, P. Chanvorachote, Regulation of lung cancer cell migration and invasion by reactive oxygen species and caveolin-1, J. Biol. Chem. 285 (50) (2010) 38832–38840.
[62] H.-Y. Hsu, T.-Y. Lin, Y.-C. Wu, S.-M. Tsao, P.-A. Hwang, Y.-W. Shih, J. Hsu, Fucoidan inhibition of lung cancer in vivo and in vitro : role of the Smurf2-dependent ubiquitin proteasome pathway in TGFβ receptor degradation, Oncotarget 5 (17) (2014) 7870–7885.